Tectonics

RESEARCH ARTICLE
10.1029/2019TC005674

Key Points:
- Structural analyses and $^{40}Ar/^{39}Ar$ geochronology reveal multiple fault reactivations accompanying subduction initiation at the Puysegur Margin
- The data show how fault motions are linked to events occurring at the Puysegur Trench and deep within continental lithosphere
- Two episodes of Late Miocene-Pliocene reverse faulting resulted in short pulses of accelerated rock uplift and topographic growth

Supporting Information:
- Supporting information S1
- Table S1
- Figure S1
- Table S2

Correspondence to:
K. A. Klepeis,
kklepeis@uvm.edu

Citation:
Klepeis, K. A., Webb, L. E., Blatchford, H. J., Jongens, R., Turnbull, R. E., & Schwartz, J. J. (2019). The age and origin of Miocene-Pliocene fault reactivations in the upper plate of an incipient subduction zone, Puysegur Margin, New Zealand. *Tectonics*, *38*. https://doi.org/10.1029/2019TC005674

Received 18 MAY 2019
Accepted 3 AUG 2019
Accepted article online 9 AUG 2019

The Age and Origin of Miocene-Pliocene Fault Reactivations in the Upper Plate of an Incipient Subduction Zone, Puysegur Margin, New Zealand

K. A. Klepeis[1], L. E. Webb[1], H. J. Blatchford[1,2], R. Jongens[3], R. E. Turnbull[4], and J. J. Schwartz[5]

[1]Department of Geology, University of Vermont, Burlington, VT, USA, [2]Now at Department of Earth Sciences, University of Minnesota, Minneapolis, MN, USA, [3]Anatoki Geoscience Ltd, Dunedin, New Zealand, [4]Dunedin Research Centre, GNS Science, Dunedin, New Zealand, [5]Department of Geological Sciences, California State University, Northridge, Northridge, CA, USA

Abstract Structural observations and $^{40}Ar/^{39}Ar$ geochronology on pseudotachylyte, mylonite, and other fault zone materials from Fiordland, New Zealand, reveal a multistage history of fault reactivation and uplift above an incipient ocean-continent subduction zone. The integrated data allow us to distinguish true fault reactivations from cases where different styles of brittle and ductile deformation happen together. Five stages of faulting record the initiation and evolution of subduction at the Puysegur Trench. Stage 1 normal faults (40–25 Ma) formed during continental rifting prior to subduction. These faults were reactivated as dextral strike-slip shear zones when subduction began at ~25 Ma. The dextral shear zones formed part of a transpressional regime (Stage 2, 25–10 Ma) that included minor reverse motion and modest uplift above the leading edge of the subducting slab as it propagated below Fiordland. At 8–7 Ma (Stage 3), trench-parallel faults accommodated the first and only episode of pure reverse motion. Reconstructions confirm that these faults formed when the slab reached mantle depths and collided with previously subducted crust. At 5–4 Ma (Stage 4), trench-parallel faults accommodated oblique-reverse motion when an oceanic ridge collided obliquely with the Puysegur Trench. Stages 3 and 4 both accelerated rock uplift and topographic growth in short pulses. A return to strike-slip motion occurred after ~4 Ma (Stage 5) when deformation localized onto the Alpine Fault. These results highlight how the rock record of faulting links displacements occurring at Earth's surface to events occurring both at the trench and deep within the lithosphere during subduction.

Plain Language Summary Subduction zones are regions where dense crust of one tectonic plate collides with and is underthrust beneath lighter crust of another plate. One aspect of determining how these plate boundaries form focuses on the response of the upper plate to the downward thrusting of material into the mantle. Understanding this response is important not only for determining how and why surface topography evolves but also for discovering the causes of fault movements, which generate earthquakes and can be distributed across space and time in complex ways. Here we use $^{40}Ar/^{39}Ar$ isotopic dating methods to reconstruct the history of faulting above a relatively young subduction zone that extends below Fiordland, New Zealand. For the first time, these data allow us to attribute specific faulting events to different causes, including the initiation of subduction, plate interactions that occurred at 100-km depth, and the collision of an oceanic ridge with the subduction zone trench. We also relate faulting to topographic growth. The study highlights how improvements in our ability to extract information from the rock record allow us to determine the origin of fault motions and to explain why many of our observations deviate from the predictions of some published models.

1. Introduction

The southern segment of the Pacific-Australian plate boundary near Fiordland, New Zealand (Figure 1a), is one of only a few places on Earth where the geomorphic response and the sequence of fault motions related to subduction initiation can be measured directly (Gurnis et al., 2004; Mao et al., 2017; Sutherland et al., 2009). Since the early Miocene, convergence between the Australian and Pacific plates has resulted in oblique subduction at the Puysegur Trench and strike-slip motion on the Alpine Fault (Figure 1a; Sutherland

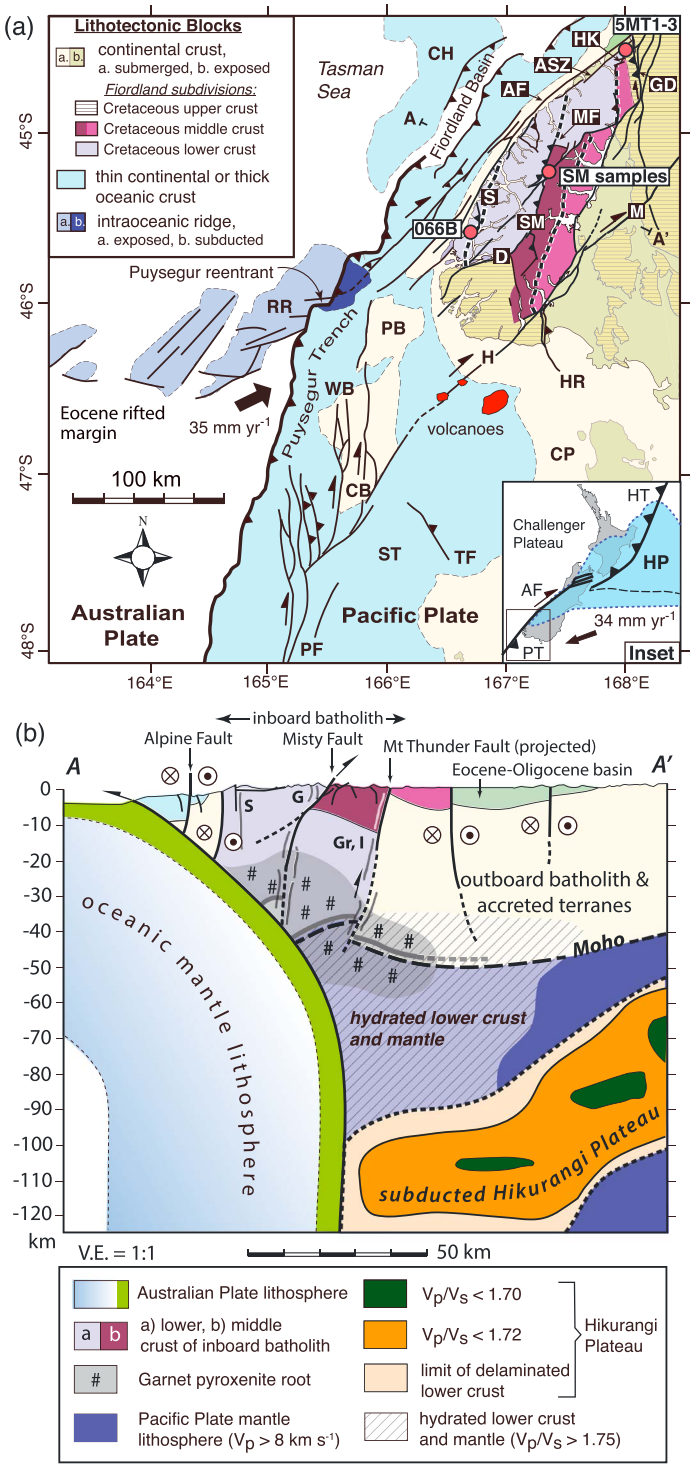

Figure 1. (a) Map of the Australian-Pacific plate boundary near Fiordland. Australian Plate motion relative to the Pacific Plate is after DeMets et al. (1994). The Median Batholith in Fiordland is subdivided into upper, middle, and lower crustal blocks (after Klepeis et al., 2019). AF = Alpine Fault; ASZ = Anita shear zone; CB = Central Balleny Fault; CH = Caswell high; CP = Challenger Plateau; D = Dusky Fault; GD = Glade-Darran Fault; H = Hauroko Fault; HK = Harrison-Kaipo fault zone; HR = Hump Ridge; M = Moonlight Fault; MF = Misty Fault; PF = Puysegur Fault; PB = Pusegur Bank; RR = Resolution Ridge; S = Straight River shear zone; SM = Spey-Mica Burn fault system; ST = Solander Trough; TF = Tauru Fault; WB = West Balleny fault zone. Circles are sampled areas. Thick black dashed lines show three crustal boundaries that coincide with the Straight River, George Sound, and Indecision Creek/Grebe shear zones. Inset shows study location (box) and velocity of the Pacific Plate relative to the Australian Plate (DeMets et al., 2010). Inset: PT = Puysegur Trench; HT = Hikurangi Trench; HP = Hikurangi Plateau (light blue). (b) Cross section (location in Figure 1a) is modified from Klepeis et al. (2019). The geometry of the subducted Australian Plate and Hikurangi Plateau is from Reyners et al. (2017). The Straight River (S), George Sound (G), Grebe (Gr), and Indecision Creek (I) shear zones are shown.

et al., 2000; Lebrun et al., 2003; Barnes et al., 2005). Here we use structural measurements and $^{40}Ar/^{39}Ar$ geochronology to determine how the upper plate of this margin responded to the inception and evolution of subduction.

Recent improvements in our ability to obtain uplift and subsidence histories from geologic records have increased our understanding of how deep-Earth processes interact with Earth's surface (e.g., Benowitz et al., 2014; Fitzgerald et al., 2014; Jiao et al., 2017; Liu et al, 2017; Warren-Smith et al., 2016). In Fiordland, Sutherland et al. (2009) showed that zones of high exhumation rates and topographic growth track the along-strike and downdip development of the subducting Australian Plate, suggesting that the subducting slab was the main driver of uplift and exhumation in the overriding plate. More recently, Mao et al. (2017) used evidence of topographic change near the Puysegur Trench to develop a two-stage model of subduction involving an initial period of fault-related uplift followed by subsidence as faulting in the upper plate ceased. These and other models that incorporate information on the rates and timing of surface change (e.g., Bendick & Ehlers, 2014; Nikolaeva et al., 2010) provide valuable predictions about the kind of deformation that is expected in the upper plate as subduction begins.

In spite of these and other advances, a major problem in trying to link episodes of topographic change to motion on individual faults in Fiordland is that most faults record a variety of deformation styles with unknown timings and durations (Turnbull et al., 2010). Hence, it is difficult to distinguish whether fault-slip directions have changed through time or if displacements were partitioned, with different types of brittle and ductile deformation occurring simultaneously in different places. High-resolution geochronology usually is required to resolve these possibilities, necessitating high-quality fault exposures and a well-defined petrologic and structural context (e.g., Eide et al., 1997; Rogowitz et al., 2015; Webb et al., 2010).

Recently, Klepeis et al. (2019) identified two zones of reverse faulting in eastern and central Fiordland that placed a block of Cretaceous lower crust up and to the east over middle and upper crust at 8–7 Ma (Figure 1a). These authors suggested that this event resulted from a deep collision between the leading edge of the subducting Australian Plate and previously subducted crust of the Cretaceous Hikurangi Plateau (Figure 1b). They also interpreted the 8- to 7-Ma event to represent the most recent in a long history of fault reactivations recorded by two crustal-scale boundaries that date back to the Carboniferous. Although their interpretations explain some of the Cenozoic uplift patterns identified by Sutherland et al. (2009), they also lead to some unresolved problems. In particular, the reverse faulting occurred some 17–18 million years after subduction began, at a time when numerical models predict that faulting in the upper plate should cease (Mao et al., 2017). Its relationship to other episodes of faulting and uplift in Fiordland is uncertain and it raises the possibility that other unreported fault reactivations also occurred. In addition to the initial coupling of the subducting slab with the upper plate at the trench interface, other postulated drivers of upper plate deformation include increased convergence rates (Cande & Stock, 2004) and ridge collisions at the Puysegur Trench (Barnes et al., 2005).

Here we address these possibilities by integrating new kinematic data with 26 $^{40}Ar/^{39}Ar$ dates on pseudotachylyte, mylonite, and a variety of minerals (hornblende, biotite, white mica, and potassium feldspar) from three fault zones that span the length of Fiordland (Figure 1a). For the first time, we document five distinctive stages of motion (Figure 2) on trench-parallel faults over the past 40 Myr. In addition, we apply an approach to interpreting apparent age spectra that builds on a large body of work showing that they can reveal the timing of both ductile and brittle deformation in reactivated fault zones (section 3.3). The use of a well-defined structural context and a variety of dated materials also allowed us to cross-check interpretations and evaluate the effects of recrystallization and/or argon loss due to multiple and/or prolonged periods of deformation. The result is a new tectonic model for the Puysegur Margin that incorporates the five fault stages and links them to other events that occurred during subduction, including periods of rock uplift and exhumation, ridge-trench collisions, and crust-mantle interactions at the base of the overriding plate.

2. Tectonic and Geologic Setting

2.1. Plate Tectonic History

During the Eocene-Oligocene, seafloor spreading between the Campbell Plateau and the Resolution Ridge (Figure 1a) was connected to a zone of transtension in SW New Zealand (Lamarche et al., 1997; Norris &

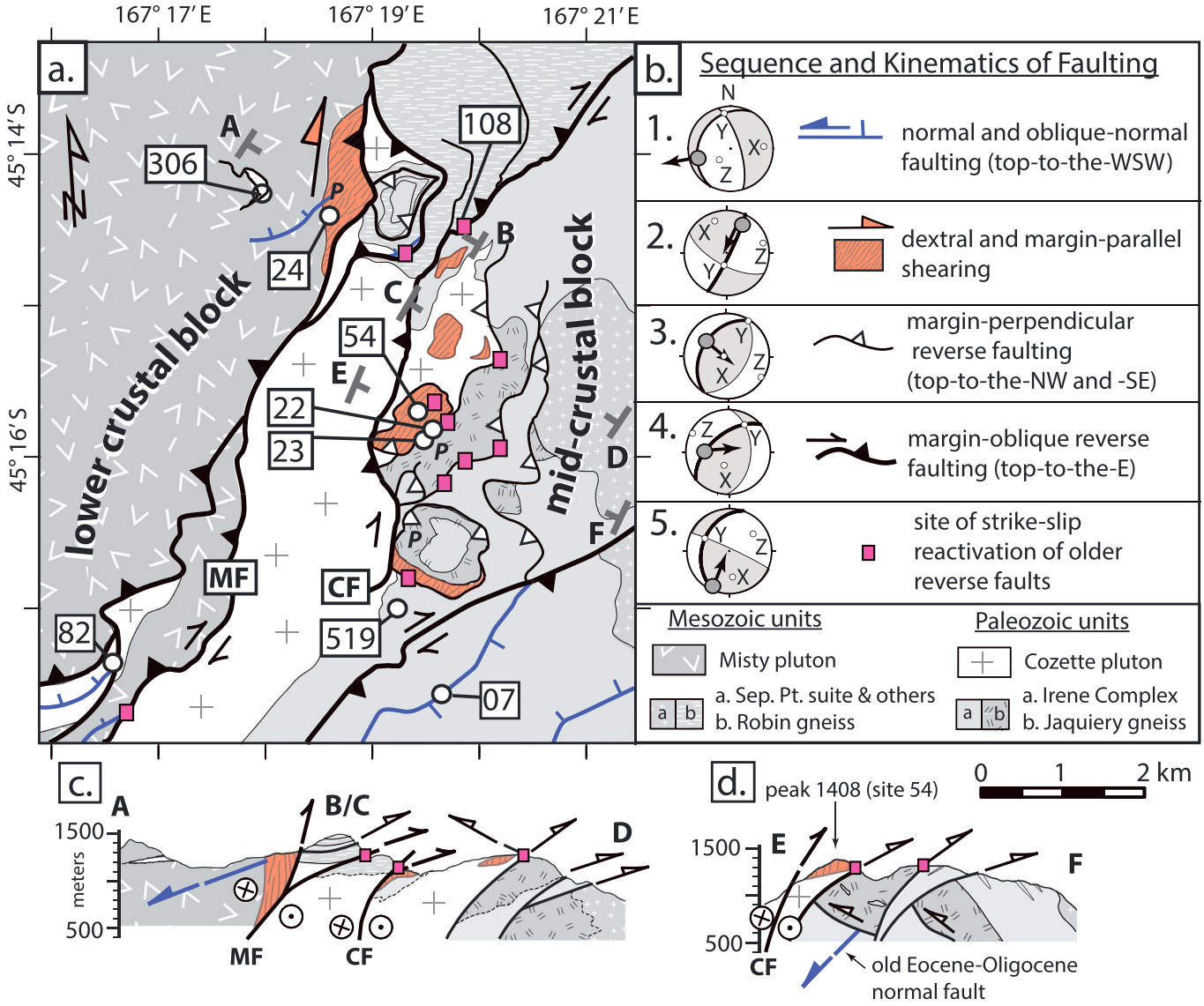

Figure 2. (a) Geological map of a part of the northern Spey-Mica Burn fault system. Boxed numbers are sample sites. MF = Misty Fault, CF = Cozette Fault. P = pseudotachylyte. (b) Sequence and kinematics of five fault stages (oldest at top). Fault plane solutions show fault orientations (thick black lines), mineral striae (dark gray dots), and the motion direction of the hanging wall (arrows). Incremental strain axes, including directions of shortening (Z) and extension (X), also are shown. Symbols to the right of each plot are used to indicate where each episode of faulting occurs on the map. A comparison of the five fault plane solutions shows the changing direction of motion on faults of similar strike (025–030°). Full data set is in Figures 5 and 6. Map shows that each successive phase of faulting truncates older generations. (c, d) Composite profile A-B and C-D and profile E-F show curved, downward steepening fault geometries (see also Figure S4 in the supporting information). White arrows show pure reverse motion. Black arrows represent oblique-reverse motion.

Turnbull, 1993). By the early Miocene, changes in relative motion between the Australian and Pacific plates caused the divergent plate boundary to reorganize, first into a zone of dextral shear and later into a zone of oblique convergence (Lebrun et al., 2003; Sutherland, 1995). These changes resulted in the subduction of Eocene-Miocene ocean crust at the Puysegur Trench and formation of the Alpine Fault (Davey & Smith, 1983; Delteil et al., 1996; Sutherland et al., 2000; Lebrun et al., 2003; Barnes et al., 2005).

The exact location, timing, and mechanism of subduction initiation are still debated. By ~23 Ma, deformation in a transpressive relay between the Puysegur and Alpine Faults (i.e., the Balleny Faults, Figure 1a; Lamarche & Lebrun, 2000; Lebrun et al., 2003) probably helped initiate subduction by localizing compression along an old fracture zone (Lebrun et al., 2003; Mao et al., 2017). This event approximately coincided with major changes in the direction and rate of Pacific-Antarctic plate motion at ~25 Ma (Cande & Stock,

2004; Jicha et al., 2018; Sutherland, 1995). Reverse motion on the Hump Ridge and Tauru Faults (Figure 1a) suggests that subduction was well underway at 16–8 Ma (Sutherland et al., 2006). Convergence rates increased throughout the Miocene from ~21 to ~34 mm/year, reaching their peak at 6–5 Ma (Cande & Stock, 2004; DeMets et al., 1994; Walcott, 1998). Between 6 and 3 Ma, a collision between the Resolution Ridge system and the Puysegur Trench localized strike-slip displacement onto the Alpine Fault and formed the Puysegur reentrant (Figure 1a; LeBrun et al., 2003; Barnes et al., 2005). During Pliocene-Quaternary time, three subduction-related volcanoes (Figure 1a) formed (Reay & Parkinson, 1997), confirming that the slab has reached mantle depths. A Benioff zone with seismicity extending to ~150-km depth also suggests a maximum of 150–200 km of total convergence (Sutherland et al., 2006). Within the last ~0.5 Ma, the Resolution Ridge has partially subducted beneath the Puysegur Trench (Barnes et al., 2005).

At present, the Alpine Fault accommodates 60–90% of the motion between the Pacific and Australian plates (Barnes et al., 2005). The absence of significant contraction across the Fiordland segment indicates that obliquely convergent motion is partitioned, with shortening being accommodated by thrust faults on either side of the Alpine Fault (Figure 1a).

2.2. Regional Geology

Fiordland is composed of Cambrian to Cretaceous plutonic rocks that intruded an Early Paleozoic metasedimentary and metavolcanic basement (Allibone et al., 2009; Turnbull et al., 2010, and references therein). These assemblages make up the Median Batholith, which consists of Carboniferous-Early Cretaceous plutons formed by arc magmatism and subduction beneath Gondwana (Allibone et al., 2009; Mortimer et al., 1999; Schwartz et al., 2017; Tulloch & Kimbrough, 2003). Exposures of the batholith can be subdivided into regions representing different crustal depths (Figure 1a; Klepeis et al., 2019). Southwest Fiordland represents Cretaceous upper crust. An eastern (outboard) belt exposes Jurassic and older plutons that were emplaced into the middle crust (Figure 1b). This midcrustal segment preserves upper and lower blocks, with deeper crust occurring west of the Cretaceous Grebe and Indecision Creek shear zones (Figures 1a and 1b). A western (inboard) belt exposes lower crust, representing the deepest part of the batholith.

2.3. Regional Structures at Depth

Beneath central and northern Fiordland, two zones of Miocene reverse faulting lie directly above a region where the subducting Australian Plate steepens to vertical against the western margin of the Hikurangi Plateau (Figure 1b; Klepeis et al., 2019). South of profile A-A′ in Figure 1a, the subducting plate parallels the Puysegur Trench and dips at ~68° below 50-km depth (Reyners et al., 2011). North of this line, the slab twists to the northeast and is vertical below 75 km (Figure 1b). The deep structure of this zone has been determined using a 3-D seismic velocity model derived from seismic tomography studies (Eberhart-Phillips et al., 2010; Reyners et al., 2017). The data reveal the subsurface extent of the plateau, which formed at ~122 Ma (Neal et al., 1997) and was partially subducted twice. The first partial subduction occurred at ~100 Ma when Fiordland was part of Gondwana; the second occurred in the late Cenozoic during convergence between the Pacific and Australian plates (Davy, 2014; Reyners et al., 2011, 2017). Currently, the plateau exists in Pacific Plate mantle as a ~35-km-thick, dipping zone of seismic activity with a layer of high Vp (~8.5 km/s) eclogite crust at its base (Eberhart-Phillips et al., 2010; Reyners et al., 2017). Its western edge is well defined at ~100 km (Figure 1b). Klepeis et al. (2019) suggested that a collision between the subducting Australian Plate and the Hikurangi Plateau resulted in Late Miocene reverse faulting above the collision zone. This interpretation serves as a hypothesis that is tested here using new structural data and geochronology.

3. Methods

3.1. Field Work and Fault Reactivation Criterion

For this study, we examined the Straight River shear zone, the northern Spey-Mica Burn fault system, and the Mt. Thunder and Glade-Darran Faults (Figure 1a). Standard field mapping techniques were used to record all observable phases of brittle and ductile deformation. These included measuring the orientations of foliations and mineral stretching lineations in ductile shear zones and determining shear sense using asymmetric structures (section 4.0). We also measured fault planes and slickenline striae and determined shear sense using offset layering, Riedel shears, and shear bands (e.g., Figures 3 and 4a). Cross-cutting

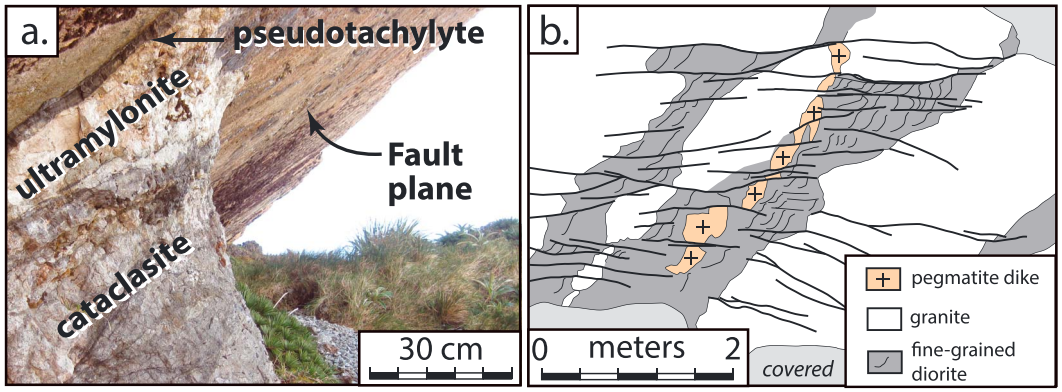

Figure 3. (a) Photograph of fault zone at Site 22 showing pseudotachylyte interlayered with ultramylonite and cataclasite (location in Figure 2a). (b) Ductile shear bands in fine-grained diorite merge with brittle faults that offset granite dikes, showing the influence of lithology on deformation mechanisms and fault style. Sense of shear is top up to the E (right). Both images are from the same fault zone. Relative locations shown in Figure S1 in the supporting information.

relationships among faults (Figure 2) and $^{40}Ar/^{39}Ar$ ages on pseudotachylyte and potassium-bearing minerals that define rock fabrics were used to establish an unambiguous sequence of deformation.

Each fault zone records multiple slip events. We use the term *fault reactivation* to describe instances where both the absolute ages and directions of motion for superposed deformation events differ significantly from one another. This criterion allowed us to distinguish cases where fault-slip patterns changed through time from those where different styles of brittle and ductile deformation occurred geologically simultaneously within the same fault zone. Examples of the latter situation occur where pseudotachylyte is interlayered with mylonite of the same age at Sites 22, 23 (Figure 3a), and 24 (Figure 5c). Additional information and photographs of the fault zones are provided in the supporting information Figures S1 and S2.

Using this criterion, we identified three different styles of fault reactivation. The first stage involved the formation of new brittle faults that truncate older brittle fault surfaces within the same fault zone (Figure 4a). The two stages are easily distinguished based on cross-cutting relationships and slickenline orientations (Figures 4b and 4c). A second style of deformation involved the superposition of ductile and semibrittle shear fabrics on top of other mostly ductile fabrics. Figure 5c illustrates this style by showing that Miocene faults reactivated an older Oligocene mylonite interlayered with Oligocene pseudotachylyte.

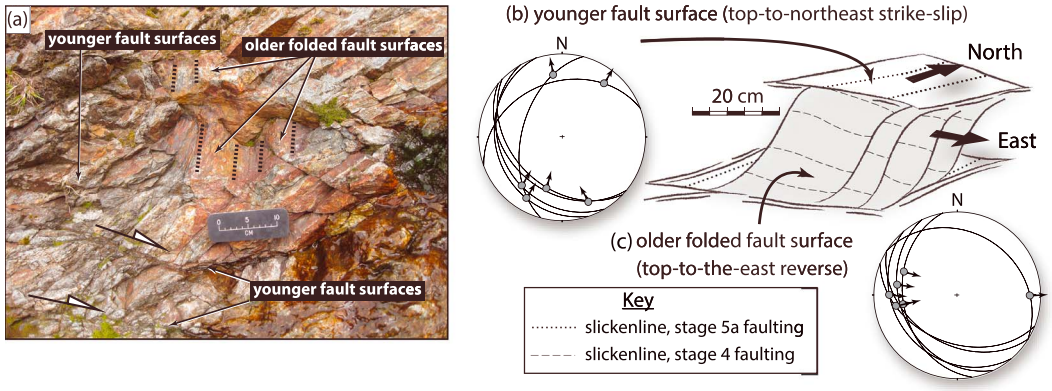

Figure 4. (a) Photograph of superposed faults at Site 108 where a younger set of Stage 5a strike-slip faults cut older (Stage 4) faults recording oblique-reverse motion. View is to the west. (b), (c) Three-dimensional sketch and lower-hemisphere, equal-area stereoplots of fault-slip data for the younger (Stage 5a) strike-slip faults that reactivate older (Stage 4) oblique-reverse faults, respectively. Great circles are fault planes, dots are slickenlines, and arrows show the direction of motion of the hanging wall for each fault. The unusual orientation of the strike-slip faults in (b) is caused by the reactivation of gently dipping fault surfaces.

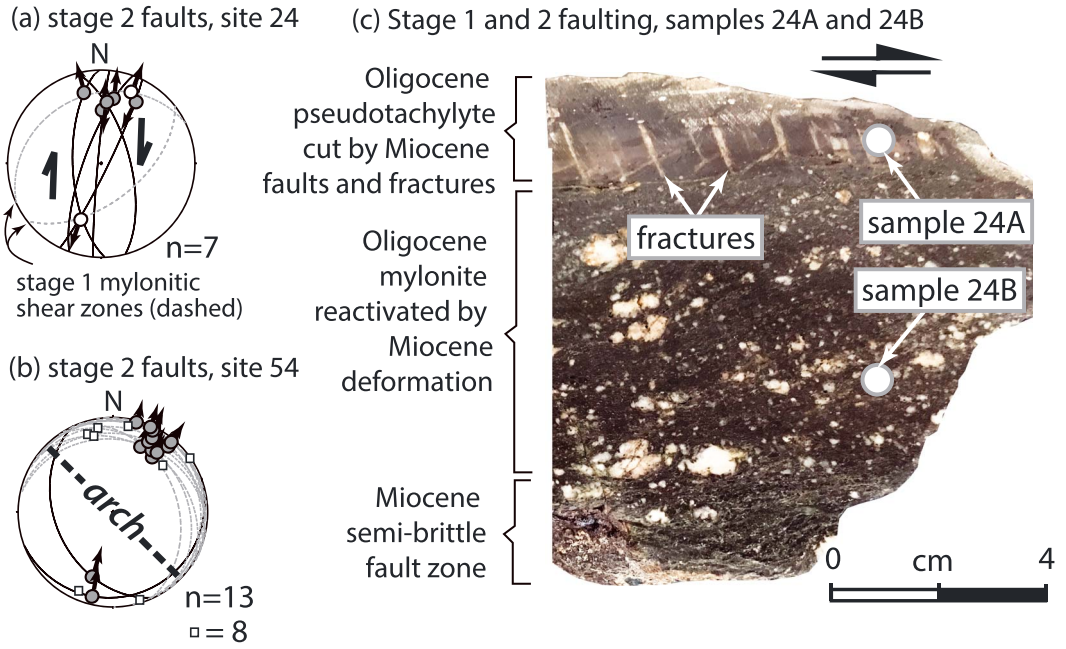

Figure 5. (a, b) Equal-area, lower-hemisphere stereoplots showing orientations of Stage 2 faults (great circles) and striae (dots) at Sites 24 and 54, respectively (northern Spey Mica Burn fault system). Locations shown in Figure 2a. Arrows show sense of motion of the hanging wall for each fault. White squares are lineations where shear sense was undetermined. Old Stage 1 (Oligocene) shear zones are shown with gray dashed great circles with white dots (slickenlines) in Figure 5a. Dashed great circles (gray) in Figure 5b show surfaces that have been tilted slightly by late-stage arching. (c) Photograph showing an Oligocene mylonite (Sample 24B) interlayered with Oligocene pseudotachylyte (Sample 24A). Both layers are reactivated by Stage 2 dextral (top-to-the-NE) faults and fractures. Age spectra and microstructures shown in Figure 7.

Third, we observed two sets of slickenlines on the same fault surface (purple squares in Figure 2). This third style involved only the last phase (Stage 5) of motion and is illustrated by Figures 6b/6f and 6c/6e, which show different directions of motion on faults of similar orientation. Where the two sets occur together, slickenlines that record strike-slip motion truncate those that record reverse motion.

3.2. Kinematic Analyses

To illustrate fault styles graphically, we plotted kinematic data on lower-hemisphere equal-area stereoplots. For faults that record mostly ductile deformation (Stages 1 and 2), great circles represent the average orientations of mylonitic foliations in high-strain zones, dots represent mineral lineations, and arrows show the sense of motion of the hanging wall (Figures 5a-5b). For faults that record mostly brittle deformation (Stages 3–5), we constructed average fault plane solutions using the methods of Marrett and Allmendinger (1990) and Allmendinger et al. (2012, and references therein). Each plot (e.g., Figure 6) shows shortening (Z) and extension (X) axes that lie at 45° from the slip direction within the shear plane. This graphical approach facilitates a rapid, qualitative comparison of the kinematics of each stage of faulting.

We also calculated the standard mean vectors of all lineation orientations for each fault set in the northern SM fault system using Fisher vector distributions and standard techniques described by Fisher et al. (1987) and Allmendinger et al. (2012); section 5). The ability to walk the traces of faults allowed us to reduce sample bias and establish that slip directions and shear senses were consistent along their length. This consistency is illustrated by the clustering of lineations on fault planes (Figure 6). The use of slickenlines allowed us to evaluate slip directions without the need to model the mechanical properties of each fault and is justified because they are widely thought to parallel the maximum resolved shear stress (or strain) on a fault plane (e.g., Angelier, 1994; Gapais et al., 2000; Sperner & Zweigel, 2010). Because slip directions collected in multiple places within each fault set are all subparallel (Figure 67), we consider the measurements to be representative and scale invariant, which is supported by observations in other fault zones (e.g., Betka et al., 2016; Marrett & Allmendinger, 1992).

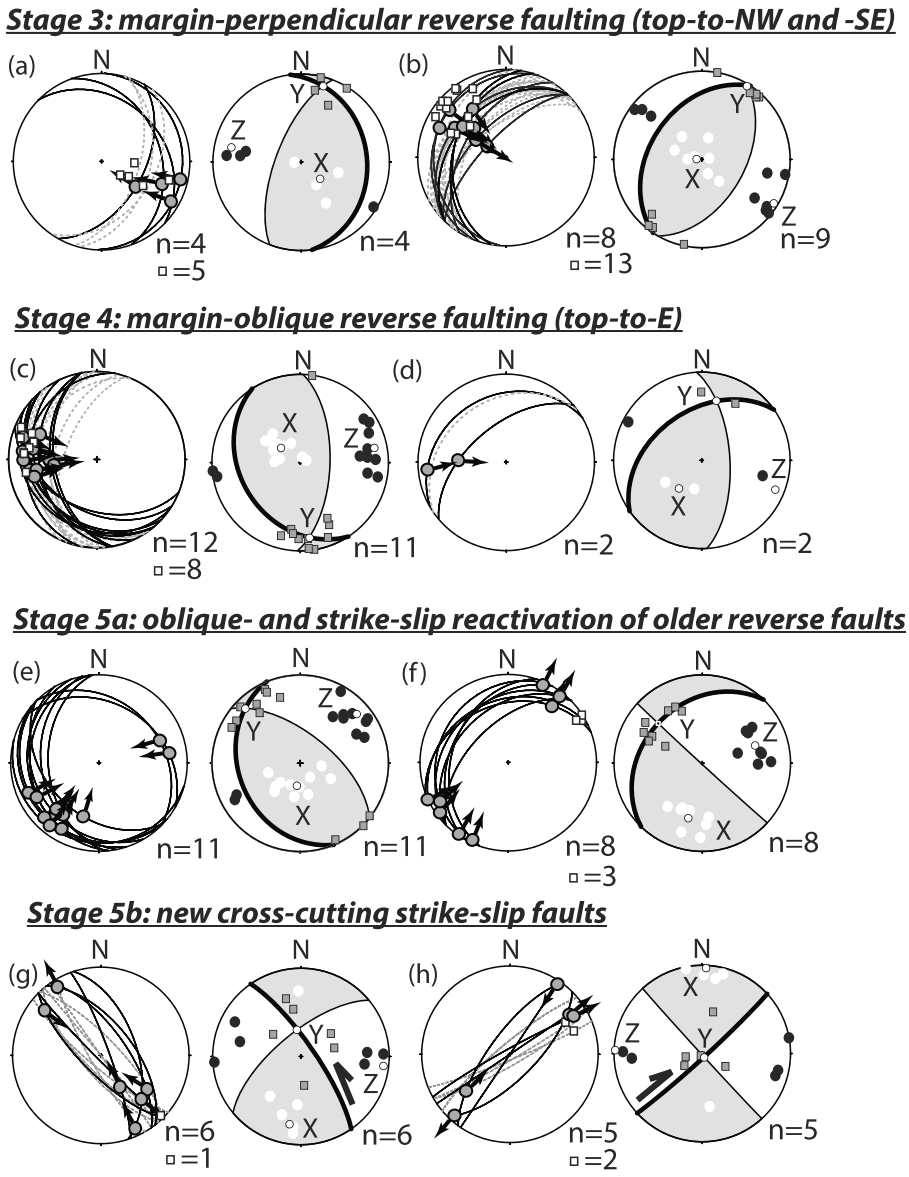

Figure 6. Stereographic projections showing orientations of faults and striae (left) and kinematic fault plane solutions (right) for fault stages 3, 4, and 5. Black great circles (fault planes) and the gray dots (slickenlines) represent areas where fault and slickenline orientations and sense of shear were obtained in the same place. White squares represent slickenlines where sense of shear was undetermined. Dashed great circles represent faults that lacked slickenlines. Figure 6c combines data from the Cozette and Misty Faults, which record similar directions and senses of motion along their lengths.

3.3. $^{40}Ar/^{39}Ar$ Geochronology

Our approach to $^{40}Ar/^{39}Ar$ geochronology builds on studies by Kirschner et al. (1996) and Dunlap (1997) who showed that deformation can play an important role in the interpretation of $^{40}Ar/^{39}Ar$ spectra because minerals commonly grow and recrystallize below their closure temperatures. Deformation commonly forms dislocations, subgrains, microfractures, and other features that facilitate fast-path diffusion and/or are prone to subsequent recrystallization, alteration, and dissolution (Lee et al., 1995; Lee & Parsons, 1995). Reddy et al. (2001) demonstrated the microstructural control on the distribution of $^{40}Ar/^{39}Ar$ apparent ages within grains and Arnaud and Eide (2000) showed that the degree of argon loss in alkali feldspar relates to deformation intensity. Similarly, biotite and white mica can record complex age spectra that reflect their

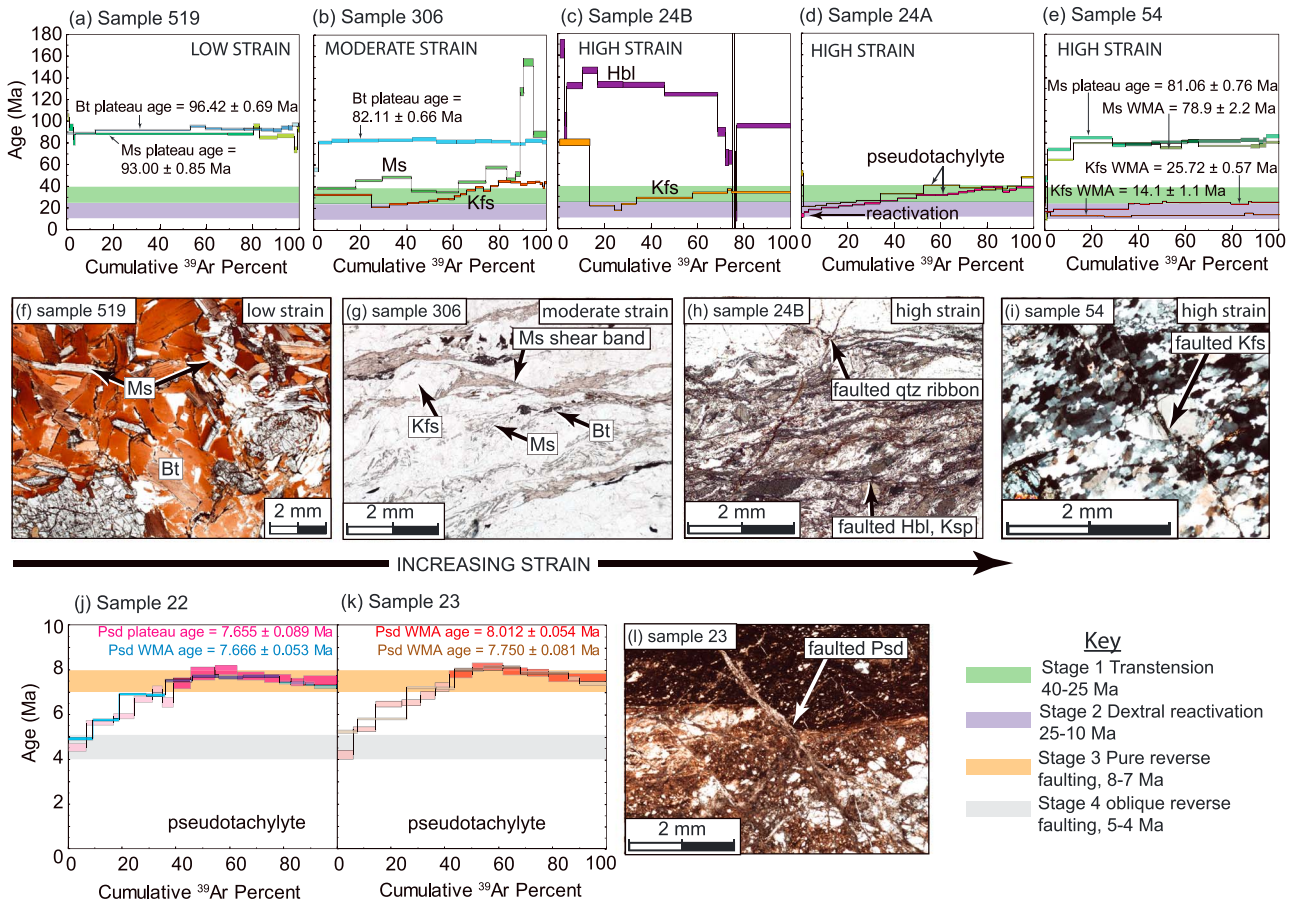

Figure 7. Diagram integrating $^{40}Ar/^{39}Ar$ spectra with sample microstructures from the northern Spey-Mica Burn fault system. Samples are arranged from low to high strain (left to right). (a–e) Argon spectra from Samples 519, 306, 24B, 24A, and 54, respectively (locations in Figure 2a). (f) Photomicrograph of Sample 519 in plane light showing coarse, intergrown biotite and muscovite in a low-strain zone. (g) Photomicrograph of Sample 306 in plane light showing muscovite shear bands around potassium feldspar augen in a moderate-strain zone. Shear sense is top to the NE (right). (h) Photomicrograph of Sample 24B in plane light (see also Figure 5c) showing faulted mylonite. Shear sense is top to the NE (right). (i) Photomicrograph of Sample 54 with crossed polars showing faulted mylonite. Matrix is composed mostly of dynamically recrystallized quartz. Shear sense is top to the NE (right). (j, k) Argon spectra from Samples 22D and 23, respectively, use data reported in Klepeis et al. (2019). (l) Photomicrograph of Sample 23 showing faulted pseudotachylyte. Hbl is hornblende, Ms is muscovite, Bt is biotite, and Ksp is potassium feldspar. Box heights of argon spectra are 1σ.

microstructural history (Baldwin & Lister, 1998; di Vincenzo et al., 2004; Forster & Lister, 2004; West & Lux, 1993) and differences in the efficiency of argon removal by fluids (Mottram et al., 2015). Meaningful $^{40}Ar/^{39}Ar$ plateau ages also have been obtained from step-heating analyses of pseudotachylyte (Magloughlin et al., 2001; Müller et al., 2002; Warr et al., 2007). This and other work (e.g., Rogowitz et al., 2015) show that argon spectra depend on mineralogy, compositional stability, and deformation. Consequently, the petrologic and structural context of a mineral can be used to determine whether to interpret apparent age spectra in the context of cooling or neocrystallization during deformation.

All step-heating analyses on minerals presented here were performed on single crystals obtained from crushing small volumes of rock representative of the thin sections analyzed for microstructures. For pseudotachylyte samples, small chips were analyzed. The $^{40}Ar/^{39}Ar$ results are summarized in Table 1. Information on sample locations, archives, and online databases are included in the supporting information. All samples were analyzed by diode laser step heating at the University of Vermont $^{40}Ar/^{39}Ar$ Geochronology Laboratory. Errors are reported at the 1σ level. Of the 26 ages reported here, six were discussed by Klepeis et al. (2019). We add new information and interpretations to these latter samples, as described in the text. Figure 11 summarizes the interpreted age intervals.

Table 1
Summary of $^{40}Ar/^{39}Ar$ Results

Sample	Phase (Aliquot)	PA (Ma)	WMA (Ma)	1σ Error (Ma)	$\%^{39}Ar$	*N* steps	MSWD	Minimum 1σ error Age (Ma)	(Ma)	$\%^{39}Ar$	*N* steps	MSWD	$\%^{40}Ar^{*}$	TFA (Ma)	1σ Error (Ma)
519	biotite	96.42		0.69	84.9	9/11	1.5	93.3	0.7	12.1	1/11		86	96.0	0.2
519	white mica	93.00		0.85	79.5	4/12	1.5	88.2	4.4	0.9	1/12		49	92.8	0.5
306	biotite	82.11		0.66	98.3	12/13	0.41	55.7	1.8	1.7	1/13		68	81.9	0.5
306	white mica							35.5	0.7	20.2	2/15	0.71	86–84	57.3	0.5
306	K-spar		44.03	0.43	19.3	6/25	1.4	21.2	0.4	7.6	1/25		100	34.4	0.2
245	hornblende							16.9	8.9	0.8	1/19		100		•
246	K-spar							17.9	0.5	2.9	1/10		81	39.3	0.4
24A	psd1							19.6	0.3	5.4	2/14	0.0049	81–64	32.1	0.1
24A	psd2							11.4	1.8	1.1	1/20		12	27.8	0.1
54	white mica1		78.9	1.1	88.1	7/9	4.4	12.8	3.4	0.9	1/9		8.4	80.6	0.6
54	white mica2	81.06		0.76	60.3	6/11	1.05	46.6	2.6	1.2	1/11		44	76.9	0.4
54	K-spar1		14.1	0.6	97.8	6/10	54	12.9	0.1	11.8	1/10		85	23.8	0.1
54	K-spar2		25.72	0.29	64.3	11/17	29	17.6	0.1	3.3	1/17		87	14.4	0.1
22	psd1	7.666	7.666	0.053	42.3	4/11	1.8	4.9	0.1	9.1	1/11		62	7.03	0.02
22	psd2	7.655		0.089	60.9	7/13	0.95	4.6	0.2	6.5	1/13		46	7.00	0.06
23	psd1		8.012	0.054	42.4	3/9	3.8	5.3	0.1	7.5	1/9		63	7.18	0.02
23	psd2		7.750	0.081	58.5	5/11	1.13	4.1	0.2	5.9	1/11		36	6.97	0.06
0666	white mica1							21.2	2.8	0.9	1/13		50	33.5	0.3
0666	white mica2		36.2	0.7	92.9	6/9	3.3	24.1	3.1	1.0	1/9		21	36.1	0.3
SMT3B	biotite1							23.5	4.8	1	1/8		45	82.3	0.7
5MT35	biatite2	165.25		0.85	81.2	8/11	1.5	91.4	2.4	1	1/11		73	161.9	0.5
SMT3B	biotite3							57.4	2.4	1	1/14		46	101	0.6
5MT35	biotite4							29.0	2.0	1	1/16		26	108.4	0.3
SMT2	psd							31	0.4	60.3	2/11	0.38	62–59	69.9	1.2
5MT3A	psd1							6.97	0.18	50.3	2/9	0.55	57–55	11.1	0.2
SMT3A	psd2							7.1	0.1	20.1	1/12		33	17.8	0.2

Note. Please see Table S1 in the supporting information for information on sample location coordinates, archive information, and IGSN and Petlab databases. All data were collected from single crystals, with the exception of pseudotachylyte samples for which small chips were analyzed. PA = plateau age, if more than three consecutive steps comprising >60% of the gas released are concordant. WMA = weighted mean age, calculated in the case where consecutive steps give similar ages but do not define a plateau. *N* steps = number of steps comprising a plateau or weighted mean age, expressed as a fraction of the total number of steps. MSWD = mean square weighted deviation; psd = pseudotachylyte; K-spar = potassium feldspar. Minimum age = age of youngest step(s); if *N* steps > 2, minimum age reported is a weighted mean age of consecutive steps. $\%^{40}Ar^{*}$ = percent radiogenic ^{40}Ar (max-min range given if *N* steps > 2). TFA = total fusion (integrated) age; black dot (•) denotes not calculated due to multiple steps with negative ages.

4. Results

4.1. Northern Spey-Mica Burn Fault System

4.1.1. Structure and Relative Chronology

The Spey-Mica Burn (SM) fault system (Figure 1a) was first defined east of Doubtful Sound where Gibson (1982) observed four subparallel faults associated with steep topography and zones of epidote and chlorite alteration. South of this sound, the faults merge with the Dusky fault (D, Figure 1a). North of the sound, it projects toward the Misty and other nearby faults (Figure 1a). Klepeis et al. (2019) considered the Misty Fault to represent the northern extension of the SM fault system. Here we show that this northern Misty Fault segment is up to 6–10 km wide and preserves five stages of Cenozoic deformation (Figure 2b). These five stages are superimposed on older, gently dipping Cretaceous and Paleozoic structures (Klepeis et al., 2019), including the Late Cretaceous extensional Mt. Irene shear zone (Scott & Cooper, 2006). For simplicity, we restrict our discussion to the Cenozoic features.

4.1.1.1. Stage 1 Normal Faults

The first stage of deformation produced high-strain zones (≤10 m thick) that deform the Cretaceous Misty Pluton and the late Carboniferous (Ramezani & Tulloch, 2009) Cozette Pluton at Site 82 (Figure 2a). These shear zones display greenschist facies alteration zones and mylonitic-ultramylonitic textures. Mineral lineations composed of quartz, biotite, and white mica plunge gently to the WSW (Figure 2b). Asymmetric microstructures, including C′ shear bands and sigmoidal feldspar porphyroclasts with asymmetric biotite tails, all show a top-down-to-the-WSW sinistral-normal sense of motion.

Several other Stage 1 normal faults occur in the northern and southeastern parts of the study area (Figure 2a). Site 24 exposes a high-strain zone where greenschist facies mylonite is interlayered with thick (2 cm) layers of pseudotachylyte (Figure 5c). This fault records a top-down-to-the-W and top-down-to-the-SW sense of shear similar to that at Site 82. To the SE (Site 07, Figure 2a), mylonite in marble horizons record top-down-to-the-SE normal displacements. These Stage 1 normal faults are themselves superimposed on Cretaceous extensional features, including the Doubtful Sound (Gibson et al., 1988; Klepeis et al., 2016) and Mt. Irene (Scott & Cooper, 2006) shear zones. The older Cretaceous fabrics are distinguishable on the basis of their high-grade (amphibolite facies) metamorphic mineral assemblages and their absolute age.

4.1.1.2. Stage 2 Dextral Strike-Slip Shear Zones

The second stage of deformation produced mylonitic and semibrittle shear zones in the northern and central parts of Figure 2a (orange zones). These shear zones cut Stage 1 mylonites at Site 24 (Figures 2a and 5c). Two principal orientations are evident, a set that strikes to the NE and dips steeply (Figure 5a) and another set that is mostly flat and strikes to the NW (Figure 5b). Site 24 (Figure 2a) exposes the former type (Figures 5a and 5c). Site 54 (Figure 2a) exposes the latter, where some late-stage arching has occurred (Figure 5b). The direction of movement on both sets is similar, involving dextral strike-slip motion on NE striking surfaces and top-to-the-NE motion on the flat N and NW striking surfaces. In regions where late-stage arching is absent, the flat, NW striking faults record reverse motion. Unlike the older oblique-normal faults, all of these shear zones record motion that approximately parallels the NE trend of the Puysegur Margin (Figure 1a).

4.1.1.3. Stage 3 Reverse Faults

Superimposed on all Stage 1 and Stage 2 shear zones are two sets of Stage 3 reverse faults, one of which dips gently to the SE and the other displays a steep, downward curving geometry (Figures 2c and 2d). The faults that dip to the NW cut those that dip to the SE (Figure 2d), indicating that the former set is younger. Both sets record pure reverse motion (Figures 6a and 6b). Together, they record NW-SE shortening perpendicular to the trend of the Puysegur Margin.

At Sites 22 and 23 (Figure 2a), pseudotachylyte layers up to 5 cm thick are in contact with a Stage 3 fault plane and are interlayered with ultramylonite and cataclasite (Figure 3a). Similar pseudotachylyte layers occur on both NW and SE dipping fault sets. Figure 3b illustrates the lithological control on the width and styles of deformation within this fault. It is widest in layers of fine-grained, mica-rich diorite and both refracts and narrows within the coarser and more competent granitic units. Ductile shear bands and folds record viscous flow in the diorite, whereas the granite deformed mostly by brittle fracture. The continuity of these structures across the layers indicates that the different styles of deformation occurred simultaneously. It also shows that the faults are neither strictly brittle nor strictly ductile.

4.1.1.4. Stage 4 Oblique-Reverse Faults

A change in the direction and style of faulting is marked by the formation of Stage 4 faults. The Cozette Fault (new name) and the Misty Fault (MF, CF, Figure 2) both cut Stage 3 structures and accommodated oblique-reverse (top-up-to-the-E) motion (Figures 4c, 6c, and 6d) on convex surfaces (Figures 2c and 2d). They also are out of sequence with respect to Stage 3 because they stepped westward, toward the trench instead of breaking NE into the foreland. Slickenlines are abundant. Kinematic indicators include C′ shear band cleavages, Reidel shears, and offset layers.

4.1.1.5. Stage 5 Strike-Slip Faults

The youngest episodes of faulting involved a return to mostly strike-slip motion. Two styles (Stages 5a and 5b) are evident (observation sites shown by purple squares in Figure 2a). First, in some areas (e.g., Site 108), the strike-slip motion is indicated by the formation of new shear surfaces (Stage 5a) that truncate Stages 3 and 4 faults (Figure 4a). The younger episode of slip is distinguished on the basis of cross cutting relationships and nearly perpendicular slickenline orientations (Figures 4b and 4c). A second style (Stage 5b) formed subvertical, conjugate-style strike-slip faults with trace lengths of at least 3–4 km and displacements of at least 50 m. The dextral set strikes to the NE (Figure 6h) parallel to the Alpine Fault. The sinistral set strikes to the NW (Figure 6g). Identical slip directions recorded by both Stages 5a and 5b faults (compare Figures 6e, 6f, and 6h) suggest that they reflect the same event.

4.1.2. Samples and $^{40}Ar/^{39}Ar$ Step Heating Results

To determine the time that Stage 1 and Stage 2 mylonites formed, we collected five samples (locations in Figure 2a) that record different strain intensities with respect to these two events. Sample 519 was

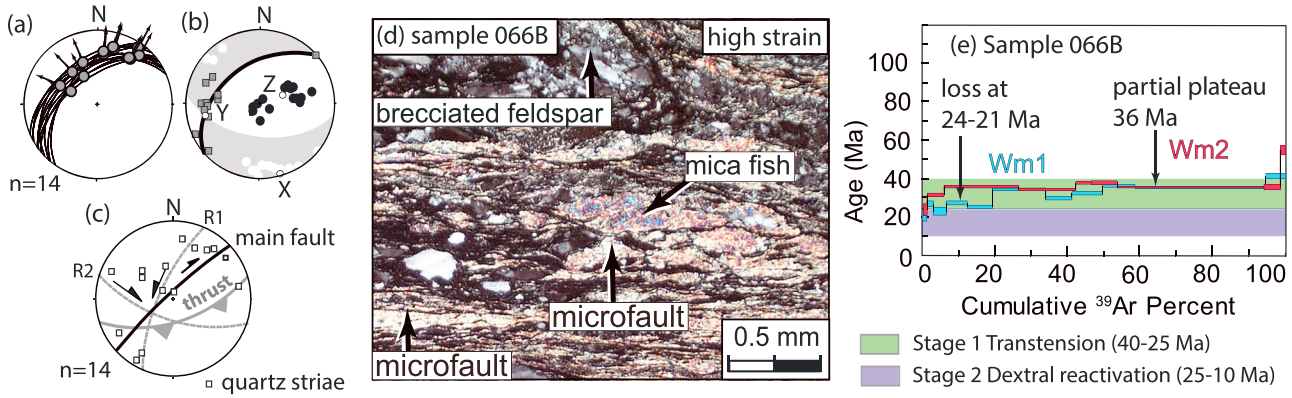

Figure 8. (a) Equal-area, lower-hemisphere stereoplot showing orientations of Stage 1 Eocene-Oligocene oblique-normal faults (great circles) and striae (dots) in the Straight River shear zone. Arrows show motion of the hanging wall for each fault. (b) Average fault plane solution for faults shown in (a). (c) Stereoplot showing orientations of Stage 2 transpressional structures that reactivated the shear zone, after King et al. (2008). Black line is the main fault, and gray lines are Reidel shears (R1 and R2). The average orientation of minor thrusts observed by King et al. (2008) also are shown. Stage 2 deformation involved dextral-reverse motion with a component of shortening across the main fault. (d) Photomicrograph of Sample 066B in polarized light showing asymmetric white mica fish surrounded by dynamically recrystallized quartz. These minerals form part of a Stage 1 foliation that is deformed by Stage 2 dextral microfaults. The image is aligned with the main fault plane shown in Figure 4c (dark black line), such that NE is to the right, SW is to the left, and the top of the image corresponds to the top of the (vertical) fault surface. (e) Plot of $^{40}Ar/^{39}Ar$ spectra from Sample 066B (location on Figure 1a). Colored bands indicating periods of transtension (Stage 1) and dextral reactivation (Stage 2) are copied from Figure 7 to facilitate comparisons.

collected from a low-strain site 0.5 km away from all studied faults and shear zones and serves as a reference point. Sample 306 is from a moderately deformed area at the margin of a Stage 1 ductile normal fault with minor reactivation by Stage 2 dextral strike-slip shear zones. Samples 24A and 24B are from a high-strain zone where both events are superimposed on one another (Figure 5c). Sample 54 is from a high-strain zone with respect to Stage 2 shearing. The structural context of these samples and our ability to date a range of materials (pseudotachylyte, biotite, muscovite, hornblende, and potassium feldspar) from them allowed us to interpret their deformation history.

Sample 519 is a garnet-mica schist from the Irene complex (Figure 2a) that shows coarse, blades of intergrown biotite and muscovite surrounding older garnet, kyanite, and andalusite porphyroblasts (Figure 7f). Fibrolitic sillimanite also is present. In most places biotite and muscovite show weak alignment. These textures support the interpretation of low strain with respect to both Stages 1 and 2. Argon spectra from biotite and muscovite (Figure 7a) in this sample yielded Late Cretaceous plateau ages of 93.00 ± 0.85 and 96.42 ± 0.69 Ma, respectively, consistent with field evidence that they escaped Stages 1 and 2 deformation.

Sample 306 is a granitic gneiss from a raft of the Carboniferous Cozette pluton within the Cretaceous Misty pluton. Muscovite and quartz form coronas and >1-cm pressure shadows around large (1–2 mm) clasts of potassium feldspar (Figure 7g). The pressure shadows are deformed into Stage 1 shear bands, indicating moderate strains. Dark clusters of matrix biotite are caught up in some, but not all, of the shear bands. The biotite yielded a plateau age of ~82 Ma (Figure 7b), suggesting that it either grew or cooled during the Late Cretaceous and does not record Stages 1–5 deformation. Muscovite yielded a spectrum dominated by Eocene ages, including two consecutive minimum ages with a weighted mean age of 35.5 Ma comprising 20.2% of the cumulative ^{39}Ar released. The pressure shadows composed of muscovite indicate that this phase grew during Stage 1 deformation. This texture, along with older ages obtained at the highest temperature steps, lead us to interpret the spectrum in terms of Eocene recrystallization of muscovite with partial preservation of domains recording Cretaceous cooling ages. We rule out an interpretation of prolonged cooling for muscovite in the Cenozoic because biotite, which has a lower closure temperature than muscovite (Braun et al., 2006), preserves a robust 82-Ma plateau age, indicating that cooling mainly occurred during the Cretaceous.

Potassium feldspar in sample 306 yielded a pattern of ages that increase from a minimum of ~21 Ma to a flatter segment with a weighted mean age of ~44 Ma over the final 19.3% of cumulative ^{39}Ar released. The spectra could reflect either cooling and/or resetting during Eocene-Oligocene transtension. However, similar ages from synkinematic muscovite and pseudotachylyte in the same shear zone and a lack of the grain

boundary area reduction textures expected for slow cooling, lend support to the latter interpretation. In addition, the preservation of old Cretaceous biotite ages, the evidence for muscovite growth, and textural evidence that potassium feldspar was not dynamically recrystallizing but quartz was (bulging recrystallization), all suggest that deformation temperatures were in the range 200–300 °C. Given that potassium feldspar generally has low closure temperatures (150–300 °C) and tends to be leaky and easily disrupted (Streepey et al., 2002), we interpret the Eocene ages in terms of deformation.

Samples 24A and 24B are from an amphibolite gneiss where pseudotachylyte is interlayered with mylonite (Figure 5c). High strains are indicated by dynamically recrystallized quartz ribbons, asymmetric tails of biotite, and muscovite around potassium feldspar augen, hornblende fish, shear bands of finely shredded biotite and muscovite, and late faults that cut all minerals (Figure 7h). A comparison of mineral textures inside and outside the shear zone indicates that the hornblende and potassium feldspar grains are inherited from the Cretaceous protolith with steps yielding Cretaceous ages. The hornblende (Figure 7c) yielded a complex apparent age spectrum consistent with a Cretaceous gneiss whose system is disturbed by a younger event. Potassium feldspar (Figure 7c) shows age gradients similar to those observed in sample 306. These are compatible with either cooling or argon loss during Stage 1 deformation at 40–30 Ma. We prefer the latter interpretation because pseudotachylyte (two runs; Figure 7d) from the same shear zone yielded identical ages (40–30 Ma), suggesting that the feldspar also records Stage 1 deformation. Younger (≤25 Ma) apparent ages from Sample 24A during the first seven to eight steps (34–41% of ^{39}Ar released) are interpreted to reflect argon loss. Evidence supporting this interpretation is that the pseudotachylyte in this sample is cut by young faults (Figure 5c), indicating a latter brittle deformation overprint.

Sample 54 is from a high-strain zone with respect to Stage 2 shearing with no visible Stage 1 deformation. The sample shows a mylonitic foliation defined by dynamically recrystallized quartz (bulging recrystallization) surrounding asymmetric augen of potassium feldspar (Figure 7i). Quartz forms oblique foliations between fine-grained biotite shear bands that record a top-to-the-NE (margin-parallel) sense of shear. Muscovite yielded argon apparent age spectra consistent with an inherited, Late Cretaceous origin (Figure 7e). One run of potassium feldspar resulted in an age gradient from a weighted mean age of 25.72 ± 0.29 Ma to a minimum age of ~18 Ma (Figure 7e). A second aliquot of potassium feldspar yielded a flatter plateau-like spectrum with a weighted mean age of 14.1 ± 0.6 Ma. Given the microstructural evidence for ductile deformation (cf. Sample 306), these spectra most likely record Stage 2 deformation. An interpretation whereby dextral shearing began at ~25 Ma and continued through ~14 Ma is compatible with the cross-cutting relationships between Stage 1 (40–30 Ma) and Stage 2 structures. It also explains why the K-feldspar ages from Sample 54 are younger than those from Stage 1 shear zones (Samples 306 and 24B).

Samples 22 and 23 are from two different layers of pseudotachylyte from a large Stage 3 reverse fault that placed a slice of the Cozette pluton to the SE over a block of granite and schist (Figure 3a). The layers are black, up to 10 cm thick, and lie in contact with the fault surface. They display clear boundaries and no injection veins. Above the fault, the granite is highly fractured with microfaults and shear bands. In contact with the upper side of the fault surface are thin (2–3 cm thick) zones of ultramylonite, above which a zone of cataclasite gradually gives way to foliated schist where asymmetric biotite and white mica show a top-to-the-SE shear sense. Decreasing quartz grain sizes suggest that strain increases downward toward the fault. The presence of interlayered pseudotachylyte and ultramylonite confirm this observation. These fault rocks preserve evidence for multiple episodes of movement, including superposed slickenlines and cross-cutting faults (e.g., Figure 7l). Slickenlines on the main fault plunge to the NW and are part of the Stage 3 faults. Slickenlines on younger slip surfaces record reactivation by Stage 4 and Stage 5a events.

In thin section (Figure 7l), pseudotachylyte is foliated and folded, indicating it flowed prior to crystallization (Fabbri et al., 2000). Clast-dominated horizons entrain rounded fragments of older pseudotachylyte, indicating multiple melt-producing events. Melt horizons are cut by narrow, epidote-rich fractures, some of which record cataclasitic flow. Very thin bands of pseudotachylyte also occur along microshear bands, indicating a mix of frictional and viscous deformation mechanisms. The argon spectra, which include replicates of both samples (first reported in Klepeis et al., 2019), are self-consistent with plateau or plateau-like segments of 7.66–8.01 Ma and strong age gradients with minimum ages of 4.1–5.3 Ma. Plots of K/Ca ratios for the different steps (supporting information) show similar values for low- and high-temperature steps, suggesting that significant chemical alteration of the glasses has not occurred. Decreasing K/Cl ratios correlated with

decreasing age could be consistent with introduction of Cl-bearing fluids along the microfaults. Based on direct evidence of faulting affecting the glasses after they formed, we infer that the minimum ages most likely reflect fault reactivation. The combined results suggest that the Stage 3 pseudotachylyte formed at 8–7 Ma followed by Stage 4 reactivation and argon loss at 5–4 Ma (Figures 7j and 7k).

4.2. Straight River Shear Zone

4.2.1. Structure and Relative Chronology

The Straight River shear zone (S, Figure 1) forms part of a 10-km-wide corridor of deformation that extends for ~200 km along the western margin of Fiordland. In the north, the corridor includes the Anita shear zone (Figure 1a), which parallels the Alpine Fault (~050°). In the south, it contains the Straight River shear zone, which parallels the Puysegur Trench (023°). The latter shear zone preserves two stages of Cenozoic deformation that are superimposed on a preexisting fabric of late Carboniferous to Early Cretaceous age (King et al., 2008). The first stage involved top-down-to-the-NW, oblique-normal motion on NW-dipping faults (Figure 8a, 8b). This deformation is brittle in places, elsewhere it is expressed in mylonitic zones composed of quartz, chlorite, muscovite, biotite, and epidote. The second stage produced steep, semibrittle faults. Minor conjugate strike-slip faults form sinistral (R1) and dextral (R2) pairs in the main fault zone (Figure 8c). Minor thrusts dip gently to the SE. King et al. (2008) showed that these latter structures form part of a zone of dextral transpression.

4.2.2. Samples and $^{40}Ar/^{39}Ar$ Step Heating Results

Sample 066B is from a high-strain zone along the main trace of the Straight River shear zone (Figure 1a). In thin section, white mica is intergrown with chlorite and forms part of a greenschist facies mylonitic foliation. Quartz ribbons are dynamically recrystallized and white mica forms asymmetric fish (Figure 8d). Late, cross cutting microfaults deform the foliation into asymmetric lozenges (Figure 8d). These textures reflect an initial transtensional phase that produced the mylonite and a second mainly brittle stage of dextral strike-slip faulting. Argon spectra (Figure 8e) from the white mica (two runs) yielded plateau segments at ~36 Ma (a weighted mean age of 36.2 $\pm$ 0.7 Ma for the second white mica aliquot). A comparison with other Stage 1 shear zones, which show similar textures and ages, suggests that the spectra most likely record either cooling or (re)crystallization during Eocene deformation (see also section 6.1). At low temperatures, multiple steps show younger apparent ages over the first 20% of ^{39}Ar released, suggesting argon loss since the Eocene.

4.3. Mt. Thunder Fault

4.3.1. Structure and Relative Chronology

The Mt. Thunder Fault (Klepeis et al., 2019) lies between the Glade-Darran and Harrison-Kaipo fault zones (Figure 1a). The Glade-Darran Fault forms the steep, NE boundary of the Fiordland massif. At its northern end, it records mainly dextral strike-slip motion on subvertical surfaces (Figure 9a) although some oblique-slip and west-side-up reverse motion also occurs. To the west, the Harrison-Kaipo fault zone (Figure 1a) separates middle to upper crustal rock of the Darran Complex from mafic, lower crustal rock of the Arthur River Complex. This latter fault zone records dextral strike-slip motion on its southern segment (Claypool et al., 2002). Farther north, it curves to the north and dips steeply to the east, forming the Kaipo Fault. Together, the Kaipo and Mt. Thunder Faults form an imbricated series involving top-up-to-the-west reverse motion on downward-steepening fault planes (Figure 9b). Claypool et al. (2002) showed that the reverse faults accommodated 3.0–5.5 km of vertical uplift that, coupled with erosion, exhumed the upper greenschist facies, mylonitic roots of the fault system. All of these faults terminate against the Alpine Fault at their northern ends.

4.3.2. Samples and $^{40}Ar/^{39}Ar$ Step Heating Results

Three samples were collected from the Mt. Thunder Fault to determine its history. Sample 5MT2 is from a pseudotachylyte (psd) layer within a hornblende- and plagioclase-rich tonalite host where old Stage 1 normal faults are visible. In thin section (Figure 9c), a sequence of at least three fault-related melting events can be determined. The oldest generation of pseudotachylyte (psd1) is 1 mm thick and contains angular clasts of the tonalitic host. Another generation (psd2) locally intrudes psd1 layers and contain clasts of the older set. Zones of ultracataclasite parallel these latter layers, indicating that they formed along faults. Both sets are cut by a series of listric normal faults showing ~ 1mm offsets and forming dominos and conjugate sets. The normal faults are cut by younger strike-slip faults that display a third set of thin (<0.5 mm to

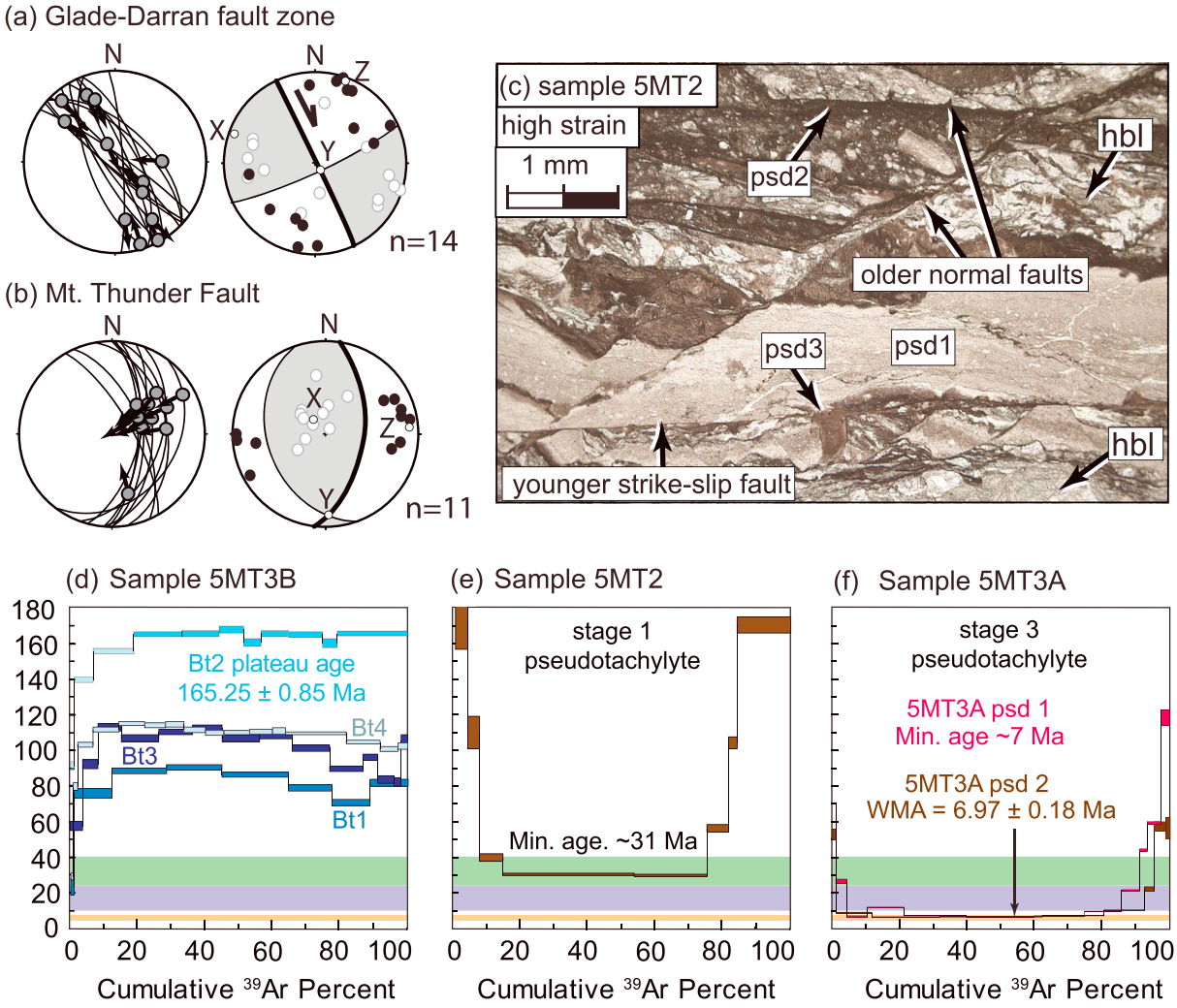

Figure 9. (a, b) Stereographic projections showing orientations of faults and striae (left) and kinematic fault plane solutions (right) for Stage 3 faults in the Glade-Darran and Mt. Thunder fault zones, respectively. Symbols are same as in Figure 6. (c) Photomicrograph showing multiple generations of pseudotachylyte (psd1–psd3) cut by Stage 1 normal faults and a younger Stage 3 strike-slip fault. Note that a pseudotachylyte layer (psd3) lies along the latter fault. (d, e) Argon spectra for Samples 5MT3B, 5MT2, and 5MT3A. Argon spectra from Sample 5MT3A are replotted using data from Klepeis et al. (2019). Colored bands are copied from Figure 7 to facilitate comparisons. Box heights of argon spectra are 1σ. Figure S3 in the supporting information provides additional data.

1.5–2 cm) pseudotachylyte layers (psd3) (Figure 9c). Sample 5MT3A is from a 2 cm thick layer of pseudotachylyte that lies within one of these young faults (Figure S3a in the supporting information).

Sample 5MT3B is a tonalitic gneiss from the fault damage zone. In thin section, metamorphic biotite forms coronas and pressure shadows around coarse, igneous plagioclase (Figure S3b in the supporting information). In places, the biotite is poorly aligned. Another, younger generation of biotite is intergrown with bands of chlorite that define small cataclastic fault zones where grain sizes have been mechanically reduced.

Biotite argon spectra from Sample 5MT3B (Figure 9d) yielded variable results, presumably due to varying degrees of heating and/or deformation postdating the Jurassic plateau age obtained from aliquot Bt2. The Jurassic age matches previously published zircon ages from the Darran Complex (Schwartz et al., 2017). The complex biotite spectra suggest either cooling or growth during Late Cretaceous rifting (Tulloch et al., 2019). Two concordant steps showing a minimum age of ~31 Ma were obtained from a thick layer of pseudotachylyte in Sample 5MT2 (Figure 9e), which is consistent with the age of Eocene-Oligocene normal faulting observed elsewhere. Two aliquots of pseudotachylyte from Sample 5MT3A in a zone of strike-slip faulting yielded minimum ages of ~7 Ma (Figure 9f; first reported by Klepeis et al., 2019). These results

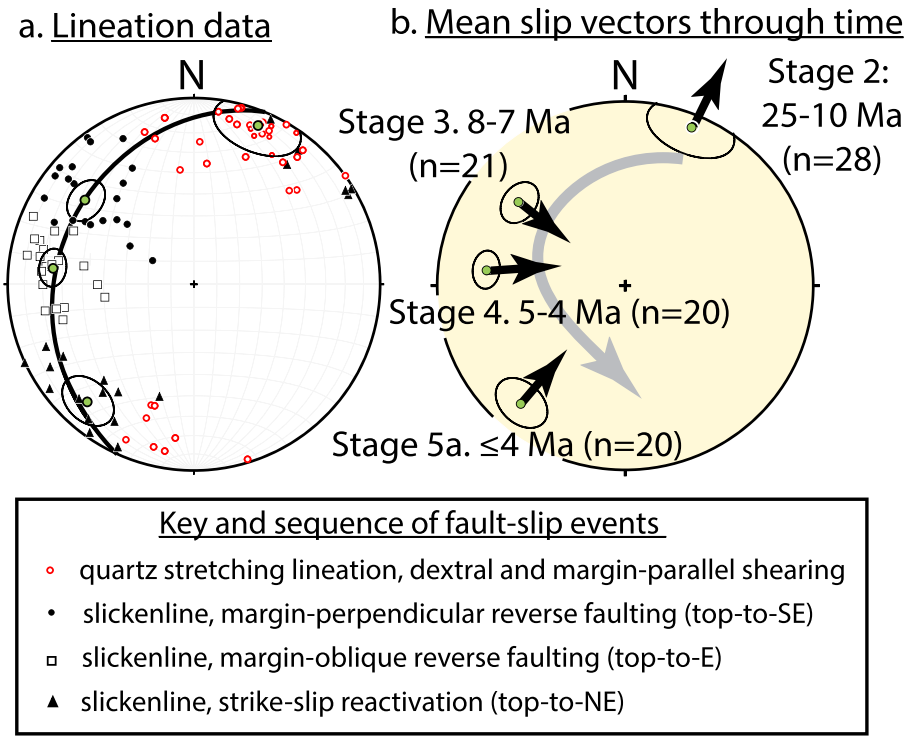

Figure 10. (a) Stereographic projection showing orientations of slickenlines and mineral lineations for Stages 2–5a slip in the northern Spey-Mica Burn fault system. Black small circles are 95% confidence intervals. See text for explanation. (b) Stereographic projection summarizing changes in mean slip vector through time (thick gray arrow) derived from information in Figure 10a and the interpreted ages of faulting (Figure 11).

match the chronology of faulting developed in the field and in thin section (e.g. Figure 9c). Together, they suggest that the Mt. Thunder Fault records Oligocene normal faulting followed by Late Miocene (Stage 3) dextral strike-slip faulting.

5. Evolution of Miocene-Pliocene Fault Motions

The sequence of faulting in the northern section of the SM fault system is especially informative because it preserves a clear record of how slip vectors and styles changed since the early Miocene. Figure 10a shows an assessment of the average slip directions recorded by all lineation data for fault Stages 2–5a. Stage 1 lineations are omitted because they represent Eocene-Oligocene rifting that predates subduction (Stage 1: 40–25 Ma). Each mean vector on the stereonet includes a 95% confidence interval (small circle) surrounding the calculated mean. The data; which match those plotted in Figures 5a, 5b, 6b, 6c, 6e and 6f; cluster into four populations that record an anticlockwise rotation of slip directions over time. The modeled fault plane (thick black line) was selected because this orientation is dominant in fault populations 3–5a (Figure 6) and its strike (023°) parallels the Puysegur Trench. The progressive change in average tectonic movement directions through time (Figure 10b) shows an evolution from margin-parallel motion (Stage 2: 25–10 Ma) to margin-perpendicular reverse motion (Stage 3: 8–7 Ma) to margin-oblique reverse motion (Stage 4: 5–4 Ma) and, finally, back to margin-parallel strike-slip motion (Stages 5a,b: ≤4 Ma). The time intervals are from Figure 11, which summarizes the chronology of faulting over the past 40 Ma.

6. Discussion

Here we interpret the causes of the five stages of Cenozoic faulting affecting the upper (Pacific) plate of the Puysegur subduction zone by integrating fault data with the plate tectonic history of the region and its history of uplift, exhumation, and topographic growth.

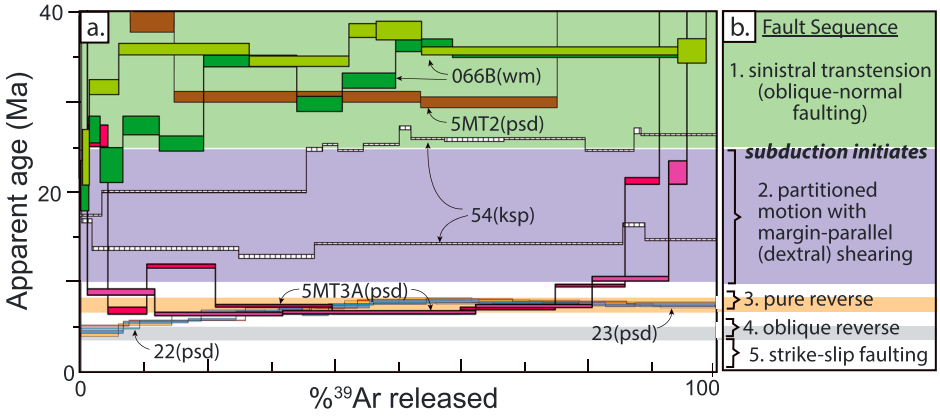

Figure 11. Summary of $^{40}Ar/^{39}Ar$ geochronology showing the five stages of faulting discussed in the text. (a) Spectra from representative samples (locations shown in Figures 1a and 2a). bt = biotite; ksp = potassium feldspar; psd = pseudotachylyte; wm = white mica. (b) Fault sequence.

6.1. Continental Rifting and Transtension

The $^{40}Ar/^{39}Ar$ ages obtained from pseudotachylyte in the northern SM fault system and Mt. Thunder fault show that normal faulting occurred at 40–30 Ma (Figure 7d) and ~31 Ma (Figure 9e) in central and northern Fiordland, respectively. These events predate subduction initiation and were coincident with the formation of extensional sedimentary basins elsewhere within and near Fiordland (Norris & Turnbull, 1993; Sutherland & Melhuish, 2000). Eocene-Oligocene muscovite ages from high-strain zones that record normal faulting in the northern SM fault system and Straight River shear zone match those from the pseudotachylyte, suggesting that Stage 1 mylonites also formed during this interval (Figures 8e and 7b–7d; sections 4.1.2 and 4.2.2). This interlayering between mylonite and pseudotachylyte with indistinguishable ages (Figure 5c) has been observed elsewhere (e.g., White, 2012; Rowe & Griffith, 2015) and appears to represent transient high-velocity slip events in regions of ductile flow. In Fiordland, Eocene-Oligocene crustal depths can be estimated by restoring the 12–15 km of Miocene uplift recorded by the Misty Fault (Klepeis et al., 2019). Together, the results suggest that Eocene-Oligocene oblique-normal faulting occurred when Fiordland's surface exposures were still relatively deep (at or below 12–15 km), warm (200–300 °C), and experiencing greenschist facies metamorphism.

The reactivation of Eocene-Oligocene normal faults during the Miocene and Pliocene in all three studied fault systems confirms that old rift structures everywhere influenced the location of younger faulting events (*cf*., Barnes et al., 2005; Sutherland et al., 2000). In addition, the Straight River shear zone shows that Eocene normal faults also reactivated a zone of Cretaceous deformation that was, itself, superimposed on a preexisting Carboniferous fabric (King et al., 2008). These superposed fabrics highlight the importance of fault zone reactivation as a means of localizing deformation during both rifting and convergence. They also support the idea (Mortimer, 2018) that a narrow corridor of pre-Cenozoic movement between North and South Zealandia helped localize deformation onto a proto-Alpine Fault.

6.2. Subduction Initiation and Transpression

The transition from the Oligocene to the Miocene marks a key period in the evolution of the Pacific-Australian plate boundary. At ~25 Ma, changes in the direction and rate of Pacific plate motion (Jicha et al., 2018) caused a divergent plate boundary to reorganize into a zone of dextral shear (Lebrun et al., 2003; Sutherland et al., 2006). The potassium feldspar spectra we obtained from the northern SM fault system (Sample 54) suggest that the first Stage 2 dextral shear zones began to form in central Fiordland at this time (Figure 11). Throughout most of the Miocene, these shear zones formed part of a dextral transpressional system that relayed motion between the Puysegur and Alpine Faults and translated material parallel to the Eocene rift margin (Lebrun et al., 2003). Our data show that the displacements were highly partitioned with dextral strike-slip motion occurring on NE-striking segments and contraction localized on short N- and NW-striking segments (Figure 12a). This result suggests that a highly oblique style of subduction began at ~25 Ma

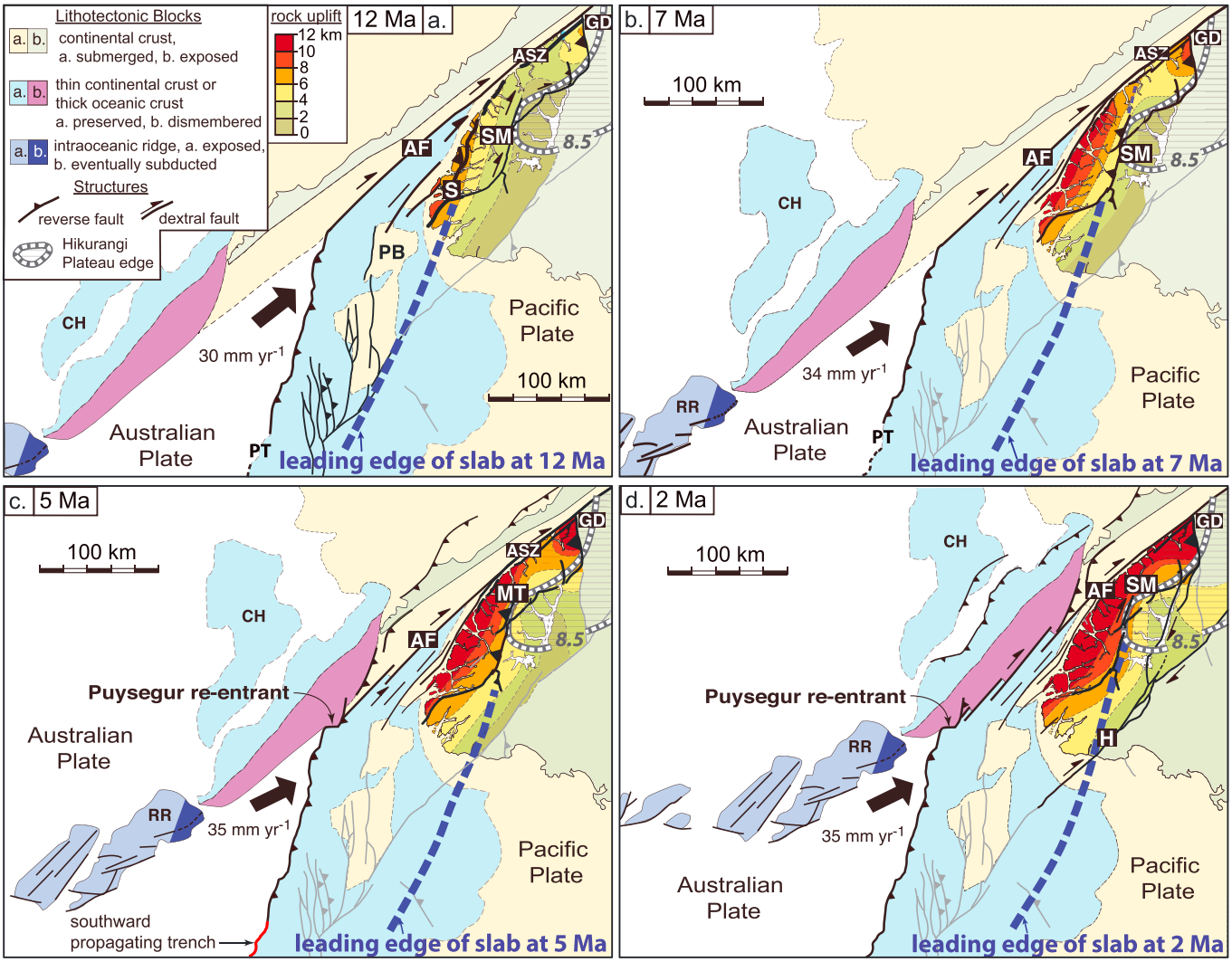

Figure 12. Plate reconstructions at (a) 12 Ma, (b) 7 Ma, (c) 5 Ma, and (d) 2 Ma. Current tectonic configuration is shown in Figure 1a. Plate motion vectors (fixed Pacific Plate) are from Cande and Stock (2004) and Sutherland et al. (2006). Offshore geometry of the plate boundary is from Barnes et al. (2005). Total rock uplift contours are from Sutherland et al. (2009). Subducted crust of the Hikurangi Plateau at ~100-km depth is shown by the isovelocity contour $Vp = 8.5$ km/s, corresponding to high velocity mantle (after Reyners et al., 2017). The position of the leading edge of the Australian slab through time is from Sutherland et al. (2009); current position is from Eberhart-Phillips et al. (2010). Black faults are active, and light gray faults are inactive; abbreviations are the same as in Figure 1. (a) At ~12 Ma rock uplift is restricted to the southwest end of western Fiordland near the Straight River shear zone. (b) At 8–7 Ma a collision between the subducting Australian plate and the edge of the Hikurangi Plateau formed reverse faults that uplifted central and northern Fiordland. (c) By ~5 Ma the Resolution Ridge system collided with the Puysegur Trench, forming the Misty and Cozette Faults. (d) By ~2 Ma reverse motion on trench-parallel faults changes back to dextral strike slip.

along a short (~40 km), NNW-striking segment of the western Puysegur Bank (Lebrun et al., 2003; Mao et al., 2017) while transpressional deformation penetrated deep into the continental interior.

By the Late Miocene, dextral transpression intensified as convergent rates increased. The history of rock uplift associated with subduction initiation allows some vertical motion to have begun as early as ~25 Ma at the SW edge of the continent (Sutherland et al., 2009). Reverse motion on the Hump Ridge and Tauru Faults south of Fiordland (Figure 1a) suggests subduction was well underway at 16–8 Ma (Sutherland et al., 2006). Sometime either before or during this latter period, the subduction front may have stepped westward onto an old Eocene fracture zone, forming the Puysegur Trench (Lebrun et al., 2003; Sutherland et al., 2006). As subduction progressed, the locus of rapid exhumation broadened and migrated toward the NE, generally following the leading edge of the subducting Australian Plate.

By ~12 Ma, the plate edge was below southwestern Fiordland, where a small, linear zone of high exhumation rates and modest uplift (House et al., 2002, 2005; Sutherland et al., 2009) had developed west of the Straight River shear zone (Figure 12a). At this locality, we observed the reactivation of the Straight River shear zone by oblique-dextral faults after Eocene-Oligocene transtension had ceased (Figures 8a–8d). The pattern suggests that the Miocene minimum ages (24–21 Ma) we obtained from muscovite at low temperatures (Sample 066B, Figure 8e) reflect argon loss during this reactivation. Alteration during deformation also may have contributed to the loss as fractures created new pathways for fluids. In support of an interpretation involving deformation, Claypool et al. (2002) used ^{40}K–^{39}Ar mineral ages on phengitic white mica to document shearing events at ~20 Ma and 13–12 Ma along this same margin, in the Anita shear zone. Simon et al. (2016) also obtained titanite ages that record multiple shearing events at 8.5 ± 3.7, 9.1 ± 1.4, 10.5 ± 0.6, and 19.0 ± 1.3 Ma. Together, these observations suggest that the entire ~200 km-long corridor of deformation in western Fiordland was reactivated by dextral faults as early as ~24 Ma, coinciding with subduction initiation and formation of the Alpine Fault. They also support an interpretation whereby Stage 2 dextral shear zones in the northern SM fault system formed at ~25 Ma and continued to develop through ~14 Ma (Sample 54).

In northern Fiordland, at this same time, a second zone of modest uplift and high exhumation rates began to form west of the Glade-Darran fault zone (Figure 12a). This fault is oblique to the rifted margin, which differs from the faults exposed farther south. The obliquity appears to have favored a larger component of reverse motion during oblique convergence. This inherited geometry also explains why the Glade-Darran Fault accumulated more vertical displacements than the trench-parallel reverse faults located farther south.

6.3. Crustal-Scale Reverse Faulting and Topographic Growth

In their study, Klepeis et al. (2019) showed that two zones of crustal-scale reverse faults lie directly above the region where the subducting Australian Plate steepens to vertical against the Hikurangi Plateau (Figure 1b). These authors suggested that the faults formed as a consequence of a Late Miocene (8–7 Ma) collision between the leading edge of the subducting Australian Plate and the western edge of the plateau at ~100-km depth. Figure 12b shows that this collision coincided with an eastward expansion of zones of rapid uplift and exhumation into eastern and northern Fiordland, suggesting that all of these events are related.

The new data sets presented here further elucidate this process by showing that the Stage 3 reverse faults mark the beginning of a brief period of pure reverse faulting in a long history of mostly oblique and margin-parallel motion. Structural analyses also show that the northern SM fault system records not one but two short-lived pulses of uplift on reverse faults. The first pulse (Stage 3), at 8–7 Ma, occurred when the leading edge of the slab first reached the southwest edge of the plateau (Figure 12b). The second (Stage 4) involved oblique-reverse motion at 5–4 Ma and coincided with a further broadening of zones of high exhumation rates into eastern and northern Fiordland (Figure 12c). Both of these episodes form part of a crustal-scale zone of uplift that developed more than 17 Ma after subduction initiated, at a time when some models predict that faulting in the upper plate should have ceased (Mao et al., 2017). These faulting events, therefore, reflect processes other than the regional shortening and dynamic uplift predicted to occur in the upper plate during the early stages of subduction initiation.

The geometric characteristics of the Stage 3 (reverse) and Stage 4 (oblique-reverse) faults provide further insight into their origins. The narrow (6–10 km) width of the SM fault system, the conjugate style of Stage 3 faults (Figures 2c and 2d), and the out-of-sequence history of Stage 4 faults all point to a system in which the forward (east-directed) propagation of fault slices was inhibited, slowing their eastward migration. Back thrusts and out-of-sequence thrusts are common in systems that "lock-up" due to resistance to further deformation. This resistance can occur where thrust blocks collide with strong preexisting structures (e.g., Klepeis, 1994; Klepeis et al., 2010) or where erosion and the lack of a décollement at depth discourage forward propagation (Konstantinovskaya & Malavieille, 2011). Furthermore, the concave, downward-steepening geometries of both fault sets (Figures 2b and 2c) indicate that they do not flatten out into a shallow décollement surface. Instead they cut through the entire crust (Figure 1b). These relationships all suggest that the two fault sets reflect a situation where the forward progress of the subducting Australian Plate was impeded by the presence of the Hikurangi Plateau. This resistance to forward motion is illustrated by a comparison of the subsurface location of the Australian slab and its present position, confirming that the slab did not migrate much farther east after ~7 Ma (Figure 12).

6.4. Ridge Subduction and Fault Zone Reactivation

When the locus of shortening and convergence near the Puysegur Bank jumped westward onto an Eocene fracture zone during the Late Miocene (Lebrun et al., 2003; Sutherland et al., 2006) the geometry of subduction changed abruptly. First, the orientation of the new trench (023°) differs from that of the older N and NW striking Balleny and Tauru Faults (Figure 1a; Barnes et al., 2005). Second, this geometric change combined with changes in relative motions caused Eocene rift fragments to be incorporated into the Puysegur Trench. Barnes et al. (2005) partially reconstructed this history of passive margin subduction and showed that the northeastern equivalents of the Resolution Ridge collided with the trench during the 6- to 3-Ma interval, creating the Puysegur reentrant (Figure 1a). Our data show that trench-parallel faults in the northern SM fault system were reactivated as oblique-reverse structures at 5–4 Ma (Figure 12c), further imbricating the crust. It also was accompanied by the north and southward growth of the Puysegur Trench and the formation of reverse faults adjacent to it (Figure 12c).

In this model, changes in the Pacific-Australian plate convergence vector promoted a ridge-trench collision, which transferred compressional stresses to the leading edge of the subducting Australian slab, causing Stage 4 oblique-reverse faulting. At this time, the slab was partially locked against the Hikurangi Plateau and probably steepened further. Furthermore, the location and orientation (i.e., trench-parallel) of the northern SM fault system inboard from the collision zone promoted its reactivation as ridge segments entered the trench. This interpretation, therefore, distinguishes the surface effects of the initial collision between the Australian Plate and the Hikurangi Plateau at 8–7 Ma (Figure 12b) from the effects of subsequent ridge-trench interactions at 5–4 Ma (Figure 12c).

6.5. Return to Strike-Slip Motion on Trench-Parallel Faults

After ~4 Ma, faults in central Fiordland were reactivated again, this time involving small amounts of dextral strike slip on trench-parallel faults (Stage 5a) followed by the formation of conjugate strike-slip pairs (Stage 5b). This result is compatible with the observations of Barnes et al. (2005) who suggested that the localization of strike-slip deformation onto the Alpine Fault was driven by the right stepping, inherited geometry of the Resolution Ridge system as it entered the Puysegur Trench. Currently, the southern Alpine Fault is principally a strike-slip fault with contraction partitioned onto reverse faults in three regions: NW of the fault (Figure 12d; Barnes et al., 2002), in northern Fiordland (Claypool et al., 2002), and across the southern South Island (Lamb et al., 2016; Norris et al., 1990). Our study also shows that the last stage (Stage 5b) of conjugate strike-slip faulting in central Fiordland (Figures 6g and 6h) records shortening at high angles to the plate boundary. These observations indicate that the beginning of the modern regime of partitioned slip began after ~4 Ma and after the subducting slab had already steepened to vertical. We speculate that the Stage 5b conjugate faults may have formed as the most recent segment of the Resolution Ridge system arrived at the Puysegur Trench within the last ~0.5 Ma, where it has partially subducted (Figure 1a).

Last, the geological history of Fiordland outlined here may help us explain why volcanism has been limited since subduction began (Figure 1a). Our model suggests that the slab had reached mantle depths by 8–7 Ma, and it seems possible that the increased crustal thickness caused by subduction of the Hikurangi Plateau has inhibited magma ascent below Fiordland. In addition, the steep orientation of the slab, which resulted from the collision (Figure 1b), may disrupt convection or dehydration processes in the mantle wedge by reducing the surface area available for fluid flux at depth. A corollary to this latter hypothesis is that the increased surface area available for fluid flux over a flat slab increases the size and volume of volcanism, which has been suggested by Brueseke et al. (2019) in Southcentral Alaska. Regardless of which of these effects may apply, the location of thee volcanoes (Figure 1a) suggests that magma ascent south of Fiordland is controlled by the Hauroko Fault, which may be similar in scale to the faults we describe.

7. Conclusions

The integration of structural data with $^{40}Ar/^{39}Ar$ geochronology reveals five stages of Cenozoic faulting within the upper (Pacific) plate of the Puysegur subduction zone. Prior to subduction (Stage 1), normal and sinistral strike-slip faults record transtension at 40–25 Ma. These faults were reactivated multiple times during subsequent stages of deformation, illustrating the importance of structural inheritance in localizing strain as the Australian-Pacific plate boundary reorganized.

Oblique subduction and formation of the Alpine Fault began at ~25 Ma, coincident with the onset of Stage 2 (25–10 Ma) transpression. This deformation was partitioned, with dextral strike-slip motion occurring on surfaces that paralleled the old Eocene rifted margin and minor reverse motion occurring on surfaces oblique to it. Transpressional shear zones continued to develop throughout the Miocene as the leading edge of the subducting Australian Plate propagated beneath Fiordland. By ~12 Ma the slab edge had reached the southern end of western Fiordland where a small, linear zone of modest rock uplift formed west of the Straight River shear zone.

During Stage 3 (8–7 Ma), the first and only episode of pure reverse faulting occurred on trench-parallel faults in the northern SM fault system and Mt. Thunder fault zone. This short-lived event coincided in space and time with a deep (~100 km) collision between the leading edge of the Australian Plate and the previously subducted Hikurangi Plateau. The deformation involved mostly vertical motion, which caused zones of rock uplift and high exhumation rates to expand suddenly into central and northern Fiordland.

During Stage 4 (5–4 Ma), the oceanic Resolution Ridge system collided obliquely with the Puysegur Trench, locally increasing interplate coupling and changing slip directions on trench-parallel faults. The collision formed two large oblique-reverse faults that further uplifted and imbricated the crust in east-central Fiordland. After ~4 Ma (Stage 5), trench-parallel faults were reactivated once again as pure strike-slip faults. New conjugate strike-slip faults also formed, marking a return to partitioned transpression where contraction occurs adjacent to the Alpine Fault.

These results highlight a multifaceted approach to determining the long-term displacement histories of continental fault zones. In particular, the ability to identify and date different types of fault reactivations allows us to link slip events to other processes associated with subduction, including subduction initiation, plate interactions at the base of the continental lithosphere, the effects of ridge-trench collisions, and transient episodes of rock uplift and topographic growth.

Acknowledgments
Funding to support this work was supported by NSF Grant EAR-1119248 and the University of Vermont Department of Geology. We thank the Department of Land Conservation in New Zealand for permission to sample. Phoebe Judge, Dan King, Alice Newman, Carson Mitchell, Kyle Titsworth, and Samantha Portnoy helped with the fault analyses. Dan Jones prepared samples and completed the $^{40}Ar/^{39}Ar$ analyses. We thank Andrew Tulloch and Nick Mortimer for discussions on New Zealand geology and tectonics. We also thank Jeffrey Benowitz and an anonymous reviewer for comments that improved the manuscript. Physical samples are archived at the University of Vermont Department of Geology and in the GNS Science collections. Sample metadata are archived online in the Geochron (http://www.geochron.org/dataset/html/geochron_dataset_2019_07_23_QJ7Xm) and Petlab (https://pet.gns.cri.nz/pet/) databases and the System for Earth Sample Registration (SESAR) http://www.geosamples.org. Sample 54 can be found at https://pet.gns.cri.nz/pet/PET_detail.jsp?ID=231721, Sample 22 can be found at https://pet.gns.cri.nz/pet/PET_detail.jsp?ID=231710, and Sample 23 can be found at https://pet.gns.cri.nz/pet/PET_detail.jsp?ID=231711.

References

Allibone, A. H., Jongens, R., Turnbull, I. M., Milan, L. A., Daczko, N. R., De Paoli, M. C., & Tulloch, A. J. (2009). Plutonic rocks of western Fiordland, New Zealand: Field relations, geochemistry, correlation, and nomenclature. *New Zealand Journal of Geology and Geophysics*, *52*(4), 379–415. https://doi.org/10.1080/00288306.2009.9518465

Allmendinger, R. W., Cardozo, N. C., & Fisher, D. M. (2012). *Structural geology algorithms—Vectors and tensors*. Cambridge, England: Cambridge University Press.

Angelier, J. (1994). Fault slip analysis and paleostress reconstruction. In P. Hancock (Ed.), *Continental Deformation* (pp. 53–100). New York: Pergamon.

Arnaud, N. O., & Eide, E. A. (2000). Brecciation-related argon redistribution in alkali feldspars: An in naturo crushing study. *Geochimica et Cosmochimica Acta*, *64*(18), 3201–3215. https://doi.org/10.1016/S0016-7037(00)00411-7

Baldwin, S. L., & Lister, G. S. (1998). Themochronology of the South Cyclades Shear Zone, Ios, Greece: Effects of ductile shear in the argon partial retention zone. *Journal of Geophysical Research*, *103*(B4), 7315–7336. https://doi.org/10.1029/97JB03106

Barnes, P., Davy, B., Sutherland, R., & Delteil, J. (2002). Frontal accretion and thrust wedge evolution under very oblique plate convergence: Fiordland Basin, New Zealand. *Basin Research*, *14*(4), 439–466. https://doi.org/10.1046/j.1365-2117.2002.00178.x

Barnes, P. M., Sutherland, R., & Delteil, J. (2005). Strike-slip structure and sedimentary basins of the southern Alpine fault, Fiordland, New Zealand. *Geological Society of America Bulletin*, *117*(3), 411–435. https://doi.org/10.1130/B25458.1

Bendick, R., & Ehlers, T. A. (2014). Extreme localized exhumation at syntaxes initiated by subduction geometry. *Geophysical Research Letters*, *41*, 5861–5867. https://doi.org/10.1002/2014GL061026

Benowitz, J. A., Layer, P. W., & Vanlaningham, S. (2014). Persistent long-term (c. 24 Ma) exhumation in the Eastern Alaska Range constrained by stacked thermochronology. *Geological Society of London*, Special Publications, *378*(1), 225–243. https://doi.org/10.1144/sp378.12

Betka, P., Klepeis, K., & Mosher, S. (2016). Fault kinematics of the Magallanes-Fagnano fault system, southern Chile; an example of diffuse strain and sinistral transtension along a continental transform margin. *Journal of Structural Geology*, *85*, 130–153. https://doi.org/10.1016/j.jsg.2016.02.001

Braun, J., van der Beek, P., & Batt, G. (2006). *Quantitative thermochronology: Numerical methods for the interpretation of thermochronological data*, (pp. 24–27). Cambridge University Press: Cambridge. ISBN 978-0-521-83057-7

Brueseke, M. E., Benowitz, J. A., Trop, J. M., Davis, K. N., Berkelhammer, S. E., Layer, P. W., & Morter, B. K. (2019). The Alaska Wrangell Arc: ~30 Ma of subduction-related magmatism along a still active arc-transform junction. *Terra Nova*, *31*, 59–66. https://doi.org/10.1111/ter.12369

Cande, S. C., & Stock, J. M. (2004). Pacific-Antarctic-Australia motion and the formation of the Macquarie Plate. *Geophysical Journal International*, *157*(1), 399–414. https://doi.org/10.1111/j.1365-246X.2004.02224.x

Claypool, A., Klepeis, K., Dockrill, B., Clarke, G., & Zwingmann, H. (2002). Structure and kinematics of oblique continental convergence in Northern Fiordland, New Zealand. *Tectonophysics*, *359*(3-4), 329–358. https://doi.org/10.1016/S0040-1951(02)00532-2

Davey, F. J., & Smith, E. G. C. (1983). The tectonic setting of the Fiordland region, south-west New Zealand. *Geophysical Journal International*, *72*(1), 23-38. https://doi.org/10.1111/j.1365-246x.1983.tb02802.x

Davy, B. (2014). Rotation and offset of the Gondwana convergent margin in the New Zealand region following Cretaceous jamming of Hikurangi Plateau large igneous province subduction. *Tectonics*, *33*, 1577–1595. https://doi.org/10.1002/2014TC003629

Delteil, J., Collot, J.-Y., Wood, R., Herzer, R., Calmant, S., Christoffel, D., et al. (1996). From strike-slip faulting to oblique subduction: A survey of the Alpine fault-Puysegur Trench transition, New Zealand, results of cruise Geodynz-sud leg 2. *Marine Geophysical Researches*, *18*(2-4), 383–399. https://doi.org/10.1007/BF00286086

DeMets, C., Gordon, R. G., & Argus, D. F. (2010). Geologically current plate motions. *Geophysical Journal International*, *181*(1), 1–80. https://doi.org/10.1111/j.1365-246X.2009.04491.x

DeMets, C., Gordon, R. G., Argus, D. F., & Stein, S. (1994). Current plate motions. *Geophysical Journal International*, *21*(20), 2191–2194. https://doi.org/10.1029/94GL02118

Di Vincenzo, G., Rocchi, S., Rossetti, F., & Storti, F. (2004). ^{40}Ar-^{39}Ar dating of pseudotachylytes: The effect of clast-hosted extraneous argon in Cenozoic fault-generated friction melts from the West Antarctic rift system. *Earth and Planetary Science Letters*, *223*(3-4), 349–364. https://doi.org/10.1016/j.epsl.2004.04.042

Dunlap, W. J. (1997). Neocrystallization or cooling? ^{40}Ar/^{39}Ar ages of white micas from low-grade mylonites. *Chemical Geology*, *143*(3-4), 181–203. https://doi.org/10.1016/S0009-2541(97)00113-7

Eberhart-Phillips, D., Reyners, M., Bannister, S., Chadwick, M., & Ellis, S. (2010). Establishing a versatile 3-D seismic velocity model for New Zealand. *Seismological Research Letters*, *81*(6), 992–1000. https://doi.org/10.1785/gssrl.81.6.992

Eide, E. A., Torsvik, T. H., & Andersen, T. B. (1997). Absolute dating of brittle fault movements: Late Permian and late Jurassic extensional fault breccias in western Norway. *Terra Nova*, *9*(3), 135–139. https://doi.org/10.1046/j.1365-3121.1997.d01-21.x

Fabbri, O., Lin, A., & Tokushige, H. (2000). Coeval formation of cataclasite and pseudotachylyte in a Miocene forearc granodiorite, southern Kyushe, Japan. *Journal of Structural Geology*, *22*(8), 1015–1025. https://doi.org/10.1016/S0191-8141(00)00021-3

Fisher, N. I., Lewis, T. L., & Embleton, B. J. (1987). *Statistical analysis of spherical data*. Cambridge, MA: Cambridge University Press. https://doi.org/10.1017/CBO9780511623059

Fitzgerald, P. G., Roeske, S. M., Benowitz, J. A., Riccio, S. J., Perry, S. E., & Armstrong, P. A. (2014). Alternating asymmetric topography of the Alaska range along the strike-slip Denali fault: Strain partitioning and lithospheric control across a terrane suture zone. *Tectonics*, *33*, 1519–1533. https://doi.org/10.1002/2013tc003432

Forster, M. A., & Lister, G. S. (2004). The interpretation of ^{40}Ar/^{39}Ar apparent age spectra produced by mixing: Application of the method of asymptotes and limits. *Journal of Structural Geology*, *26*(2), 287–305. https://doi.org/10.1016/j.jsg.2003.10.004

Gapais, D., Cobbold, P. R., Bourgeois, O., Rouby, D., & de Urreiztieta, M. (2000). Tectonic significance of fault-slip data. *Journal of Structural Geology*, *22*(7), 881–888. https://doi.org/10.1016/S0191-8141(00)00015-8

Gibson, G. M. (1982). Polyphase deformation and its relation to metamorphic crystallization in rocks at Wilmot Pass, central Fiordland. *New Zealand Journal of Geology and Geophysics*, *25*(1), 45–65. https://doi.org/10.1080/00288306.1982.10422504

Gibson, G. M., McDougall, I., & Ireland, T. R. (1988). Age constraints on metamorphism and the development of a metamorphic core complex in Fiordland, southern New Zealand. *Geology*, *16*(5), 405–408. https://doi.org/10.1130/0091-7613(1988)016<0405:ACOMAT>2.3.CO;2

Gurnis, M., Hall, C. E., & Lavier, L. L. (2004). Evolving force balance during incipient subduction. *Geochemistry, Geophysics, Geosystems*, *5*, Q07001. https://doi.org/10.1029/2003GC000681

House, M. A., Gurnis, M., Kamp, P. J. J., & Sutherland, R. (2002). Uplift in the Fiordland region, New Zealand; implications for incipient subduction. *Science*, *297*(5589), 2038–2041. https://doi.org/10.1126/science.1075328

House, M. A., Gurnis, M., Sutherland, R., & Kamp, P. J. J. (2005). Patterns of late Cenozoic exhumation deduced from apatite and zircon U-He ages from Fiordland, New Zealand. *Geochemistry, Geophysics, Geosystems*, *6*, Q09013. https://doi.org/10.1029/2005GC000968

Jiao, R., Herman, F., & Seward, D. (2017). Late Cenozoic exhumation model of New Zealand: Impacts from tectonics and climate. *Earth-Science Reviews*, *166*, 286–298. https://doi.org/10.1016/j.earscirev.2017.01.003

Jicha, B. R., Garcia, M. O., & Wessel, P. (2018). Mid-Cenozoic Pacific plate motion change: Implications for the Northwest Hawaiian Ridge and circum-Pacific. *Geology*, *46*(11), 939–942. https://doi.org/10.1130/G45175.1

King, D. S., Klepeis, K. A., Goldstein, A. G., Gehrels, G. E., & Clarke, G. L. (2008). The initiation and evolution of the transpressional Straight River shear zone, central Fiordland, New Zealand. *Journal of Structural Geology*, *30*(4), 410–430. https://doi.org/10.1016/j.jsg.2007.12.004

Kirschner, D. L., Cosca, M. A., Masson, H., & Hunziker, J. C. (1996). Staircase ^{40}Ar/^{39}Ar spectra of fine-grained white mica: Timing and duration of deformation and empirical constraints on argon diffusion. *Geology*, *24*(8), 747–750. https://doi.org/10.1130/0091-7613(1996)024<0747:SAASOF>2.3.CO;2

Klepeis, K., Betka, P., Clarke, G., Fanning, M., Hervé, F., Rojas, L., et al. (2010). Continental underthrusting and obduction during the Cretaceous closure of the Rocas Verdes rift basin, Cordillera Darwin, Patagonian Andes. *Tectonics*, *29*, TC3014. https://doi.org/10.1029/2009TC002610

Klepeis, K., Webb, L., Blatchford, H., Schwartz, J., Jongens, R., Turnbull, R., & Stowell, H. (2019). Deep slab collision during Miocene subduction causes uplift along crustal-scale reverse faults in Fiordland, New Zealand. *GSA Today*, *29*. https://doi.org/10.1130/GSATG399A.1

Klepeis, K. A. (1994). Relationship between uplift of the metamorphic core of the southernmost Andes and shortening in the Magallanes foreland fold and thrust belt, Tierra del Fuego, Chile. *Tectonics*, *13*(4), 882–904. https://doi.org/10.1029/94TC00628

Klepeis, K. A., Schwartz, J., Stowell, H., & Tulloch, A. (2016). Gneiss domes, vertical and horizontal mass transfer, and the initiation of extension in the hot lower crustal root of a continental arc, Fiordland, New Zealand. *Lithosphere*, *8*(2), 116–140. https://doi.org/10.1130/L490.1

Konstantinovskaya, E., & Malavieille, J. (2011). Thrust wedges with décollement levels and syntectonic erosion: A view from analog models. *Tectonophysics*, *502*(3-4), 336–350. https://doi.org/10.1016/j.tecto.2011.01.020

Lamarche, G., Collot, J. -Y., Wood, R. A., Sosson, M., Sutherland, R., & Delteil, J. (1997). The Oligocene-Miocene Pacific-Australia plate boundary, south of New Zealand: Evolution from oceanic spreading to strike-slip faulting. *Earth and Planetary Science Letters*, *148*(1-2), 129–139. https://doi.org/10.1016/S0012-821X(97)00026-5

Lamarche, G., & Lebrun, J.-F. (2000). Transition from strike-slip faulting to oblique subduction: Active tectonics at the Puysegur Margin, South New Zealand. *Tectonophysics*, *316*(1-2), 67–89. https://doi.org/10.1016/S0040-1951(99)00232-2

Lamb, S., Mortimer, N., Smith, E., & Turner, G. (2016). Focusing of relative plate motion at a continental transform fault: Cenozoic dextral displacement >700 km on New Zealand's Alpine Fault, reversing >225 km of Late Cretaceous sinistral motion. *Geochemistry, Geophysics, Geosystems*, *17*, 1197–1213. https://doi.org/10.1002/2015GC006225

Lebrun, J. -F., Lamarche, G., & Collot, J.-Y. (2003). Subduction initiation at a strike-slip plate boundary: The Cenozoic Pacific-Australian plate boundary south of New Zealand. *Journal of Geophysical Research*, *108*(B9), 2453. https://doi.org/10.1029/2002JB002041

Lee, M. R., & Parsons, I. (1995). Microtextural controls of weathering of perthitic alkali feldspars. *Geochimica et Cosmochimica Acta*, *59*(21), 4465–4488. https://doi.org/10.1016/0016-7037(95)00255-X

Lee, M. R., Waldron, K. A., & Parsons, I. (1995). Exsolution and alteration microtextures in alkali feldspar phenocrysts from the Shap granite. *Mineralogical Magazine*, *59*(394), 63–78. https://doi.org/10.1180/minmag.1995.59.394.06

Liu, S., Gurnis, M., Ma, P., & Zhang, B. (2017). Reconstruction of northeast Asian deformation integrated with western Pacific plate subduction since 200 Ma. *Earth-Science Reviews*, *175*, 114–142. https://doi.org/10.1016/j.earscirev.2017.10.012

Magloughlin, J. F., Hall, C. M., & van der Pluijm, B. A. (2001). ^{40}Ar-^{39}Ar geochronometry of pseudotachylytes by vacuum encapsulation: North Cascade Mountains, Washington, USA. *Geology*, *29*(1), 51–54. https://doi.org/10.1130/0091-7613(2001)029<0051:AAGOPB>2.0.CO;2

Mao, X., Gurnis, M., & May, D. A. (2017). Subduction initiation with vertical lithospheric heterogeneities and new fault formation. *Geophysical Research Letters*, *44*, 11,349–11,356. https://doi.org/10.1002/2017GL075389

Marrett, R., & Allmendinger, R. (1990). Kinematic analysis of fault-slip data. *Journal of Structural Geology*, *12*(8), 973–986. https://doi.org/10.1016/0191-8141(90)90093-E

Marrett, R., & Allmendinger, R. W. (1992). Amount of extension on "small" faults: An example from the Viking graben. *Geology*, *20*(1), 47–50. https://doi.org/10.1130/0091-7613(1992)020<0047:AOEOSF>2.3.CO;2

Mortimer, N. (2018). Evidence for a pre-Eocene proto-Alpine Fault through Zealandia. *New Zealand Journal of Geology and Geophysics*, *61*(3), 251–259. https://doi.org/10.1080/00288306.2018.1434211

Mortimer, N., Tulloch, A. J., Spark, R. N., Walker, N. W., Ladley, E., Allibone, A., & Kimbrough, D. L. (1999). Overview of the Median Batholith, New Zealand: A new interpretation of the geology of the Median Tectonic Zone and adjacent rocks. *Journal of African Earth Sciences*, *29*(1), 257–268. https://doi.org/10.1016/S0899-5362(99)00095-0

Mottram, C. M., Warren, C. J., Halton, A. M., Kelley, S. P., & Harris, N. B. W. (2015). Argon behaviour in an inverted Barrovian sequence, Sikkim Himalaya: The consequences of temperature and timescale on ^{40}Ar/^{39}Ar mica geochronology. *Lithos*, *238*, 37–51. https://doi.org/10.1016/j.lithos.2015.08.018

Müller, W., Kelley, S. P., & Villa, I. M. (2002). Dating fault-generated pseudotachylites: Comparison of ^{40}Ar/^{39}Ar stepwise-heating, laser ablation and Rb-Sr microsampling analyses. *Contributions to Mineralogy and Petrology*, *144*(1), 57–77. https://doi.org/10.1007/s00410-002-0381-6

Neal, C. R., Mahoney, J. J., Kroenke, L. W., Duncan, R. A., & Petterson, M. G. (1997). The Ontong Java Plateau. In J. J. Mahoney, & M. F. Coffin (Eds.), *Large igneous provinces, geophysical monograph series*, (Vol. 100, pp. 183–216). Washington, DC: American Geophysical Union.

Nikolaeva, K., Gerya, T. V., & Marques, F. O. (2010). Subduction initiation at passive margins: Numerical modeling. *Journal of Geophysical Research*, *115*(B3), B03406. https://doi.org/10.1029/2009JB006549

Norris, R. J., Koons, P. O., & Cooper, A. F. (1990). The obliquely-convergent plate boundary in the South Island of New Zealand: Implications for ancient collision zones. *Journal of Structural Geology*, *12*(5-6), 715–725. https://doi.org/10.1016/0191-8141(90)90084-C

Norris, R. J., & Turnbull, I. M. (1993). Cenozoic basins adjacent to an evolving transform plate boundary, southwest New Zealand. In P. F. Balance (Ed.), *South Pacific Sedimentary Basins of the World*, (Vol. 2, pp. 251–270). New York, NY: Elsevier.

Ramezani, J., & Tulloch, A. J. (2009). TIMS U-Pb geochronology of southern and eastern Fiordland. http://data.gns.cri.nz/paperdata/index.jsp, https://doi.org/10.21420/G2CC7Z

Reay, A., & Parkinson, D. (1997). Adakites from Solander Island, New Zealand. *New Zealand Journal of Geology and Geophysics*, *40*(2), 121–126. https://doi.org/10.1080/00288306.1997.9514746

Reddy, S. M., Potts, G. J., & Kelley, S. P. (2001). ^{40}Ar/^{39}Ar ages in deformed potassium feldspar: Evidence of microstructural control on Ar isotope systematics. *Contributions to Mineralogy and Petrology*, *141*(2), 186–200. https://doi.org/10.1007/s004100000227

Reyners, M., Eberhart-Philips, D., Upton, P., & Gubbins, D. (2017). Three-dimensional imaging of impact of a large igneous province with a subduction zone. *Earth and Planetary Science Letters*, *460*, 143–151. https://doi.org/10.1016/j.epsl.2016.12.025

Reyners, M., Eberhart-Phillips, D., & Bannister, S. (2011). Tracking repeated subduction of the Hikurangi Plateau beneath New Zealand. *Earth and Planetary Science Letters*, *311*(1-2), 165–171. https://doi.org/10.1016/j.epsl.2011.09.011

Rogowitz, A., Huet, B., Schneider, D., & Grasemann, B. (2015). Influence of high strain rate deformation on ^{40}Ar/^{39}Ar mica ages from marble mylonites (Syros, Greece). *Lithosphere*, *7*(5), 535–540. https://doi.org/10.1130/L455.1

Rowe, C. D., & Griffith, W. A. (2015). Do faults preserve a record of seismic slip: A second opinion. *Journal of Structural Geology*, *78*, 1–26. https://doi.org/10.1016/j.jsg.2015.06.006

Schwartz, J. J., Klepeis, K. A., Sadorski, J. F., Stowell, H. H., Tulloch, A. J., & Coble, M. A. (2017). The tempo of continental arc construction in the Mesozoic Median Batholith, Fiordland, New Zealand. *Lithosphere*, *9*(3), 343–365. https://doi.org/10.1130/L610.1

Scott, J. M., & Cooper, A. F. (2006). Early Cretaceous extensional exhumation of the lower crust of a magmatic arc: Evidence from the Mount Irene Shear Zone, Fiordland, New Zealand. *Tectonics*, *25*, TC3018. https://doi.org/10.1029/2005TC001890

Simon, I. J-P., Schwartz, J., Klepeis, K., Stowell, H., & Kylander-Clark, A. (2016). Direct dating of exhumational fabrics in the Anita shear zone, Fiordland New Zealand. Paper presented at Geological Society of America Abstracts with Programs, 48(7), Denver: Colorado. https://doi.org/10.1130/abs/2016AM-287043

Sperner, B., & Zweigel, P. (2010). A plea for more caution in fault-slip analysis. *Tectonophysics*, *482*(1-4), 29–41. https://doi.org/10.1016/j.tecto.2009.07.019

Streepey, M. M., Hall, C. M., & van der Pluijm, B. A. (2002). The40Ar-39Ar laser analysis of K-feldspar: Constraints on the uplift history of the Grenville Province in Ontario and New York. *Journal of Geophysical Research Solid Earth*ECV 12-1-ECV 12-11, , *107*(B11), 2296. https://doi.org/10.1029/2001jb001094

Sutherland, R. (1995). The Australia-Pacific boundary and Cenozoic plate motions in the SW Pacific; some constraints from Geosat data. *Tectonics*, *14*(4), 819–831. https://doi.org/10.1029/95TC00930

Sutherland, R., Barnes, P. M., & Uruski, C. (2006). Miocene-Recent deformation, surface elevation, and volcanic intrusion of the overriding plate during subduction initiation, offshore southern Fiordland, Puysegur margin, southwest New Zealand. *New Zealand Journal of Geology and Geophysics*, *49*(1), 131–149. https://doi.org/10.1080/00288306.2006.9515154

Sutherland, R., Davey, F., & Beavan, J. (2000). Kinematics of plate boundary deformation in South Island, New Zealand, is related to inherited lithospheric structure. *Earth and Planetary Science Letters*, *177*(3-4), 141–151. https://doi.org/10.1016/S0012-821X(00)00043-1

Sutherland, R., Gurnis, M., Kamp, P. J. J., & House, M. A. (2009). Regional exhumation history of brittle crust during subduction initiation, Fiordland, southwest New Zealand, and implications for thermochronologic sampling and analysis strategies. *Geosphere*, *5*(5), 409–425. https://doi.org/10.1130/GES00225.1

Sutherland, R., & Melhuish, A. (2000). Formation and evolution of the Solander Basin, southwestern South Island, New Zealand, controlled by a major fault in continental crust and upper mantle. *Tectonics*, *19*(1), 44–61. https://doi.org/10.1029/1999TC900048

Tulloch, A. J., & Kimbrough, D. L. (2003). Paired plutonic belts in convergent margins and the development of high Sr/Y magmatism: Peninsular Ranges batholith of Baja-California and Median batholith of New Zealand. In S. E. Johnson, S. R. Paterson, J. M. Fletcher, G. H. Girty, D. L. Kimbrough, & A. Martín-Barajas (Eds.), *Tectonic evolution of northwestern México and the southwestern USA*, *Geological Society of America Special Paper*, (Vol. 374, pp. 275–295). Boulder, Colorado: Geological Society of America.

Tulloch, A. J., Mortimer, N., Ireland, T. R., Waight, T. E., Maas, R., Palin, J. M., et al. (2019). Reconnaissance basement geology and tectonics of South Zealandia. *Tectonics*, *38*(2), 516–551. https://doi.org/10.1029/2018TC005116

Turnbull, I. M., Allibone, A. H., & Jongens, R. (2010). Geology of the Fiordland area: Institute of Geological and Nuclear Sciences, Lower Hutt, New Zealand, scale 1:250 000, sheet 17, 97 p. text.

Walcott, R. I. (1998). Modes of oblique compression: Late Cenozoic tectonics of the South Island of New Zealand. *Reviews of Geophysics*, *36*(1), 1–26. https://doi.org/10.1029/97RG03084

Warr, L. N., van der Pluijm, B. A., & Tourscher, S. (2007). The age and depth of exhumed friction melts along the Alpine fault, New Zealand. *Geology*, *35*(7), 603–606. https://doi.org/10.1130/G23541A.1

Warren-Smith, E., Lamb, S., Seward, D., Smith, E., Herman, F., & Stern, T. (2016). Thermochronological evidence of a low-angle, mid-crustal detachment plane beneath the central South Island, New Zealand. *Geochemistry Geophysics Geosystems*, *17*(10), 4212–4235. https://doi.org/10.1002/2016GC006402

Webb, L. E., Johnson, C. L., & Minjin, C. (2010). Late Triassic sinistral shear in the East Gobi Fault Zone, Mongolia. *Tectonophysics*, *495*(3-4), 246–255. https://doi.org/10.1016/j.tecto.2010.09.033

West, D. P. Jr., & Lux, D. R. (1993). Dating mylonitic deformation by the ^{40}Ar-^{39}Ar method: An example from the Norumbega Fault Zone, Maine. *Earth and Planetary Science Letters*, *120*(3-4), 221–237. https://doi.org/10.1016/0012-821X(93)90241-Z

White, J. C. (2012). Paradoxical pseudotachylyte—Fault melt outside the seismogenic zone. *Journal of Structural Geology*, *38*, 11–20. https://doi.org/10.1016/j.jsg.2011.11.016

References From the Supporting Information

Jicha, B. R., & Brown, F. H. (2014). An age for the Korath Range, Ethiopia and the viability of ^{40}Ar/^{39}Ar dating of kaersutite in Late Pleistocene volcanics. *Quaternary Geochronology*, *21*, 53–57. https://doi.org/10.1016/j.quageo.2013.03.007

Kuiper, K. F., Deino, A., Hilgen, F. J., Krijgsman, W., Renne, P. R., & Wijbrans, A. J. (2008). Synchronizing rock clocks of Earth history. *Science*, *320*(5875), 500–504. https://doi.org/10.1126/science.1154339

Lee, J. Y., Marti, K., Severinghaus, J. P., Kawamura, K., Yoo, H. S., Lee, J. B., & Kim, J. S. (2006). A redetermination of the isotopic abundances of atmospheric Ar. *Geochimica et Cosmochimica Acta*, *70*(17), 4507–4512. https://doi.org/10.1016/j.gca.2006.06.1563

Ludwig, K. R. (2003). Isoplot/EX, rev. 3.00, a geochronological toolkit for Microsoft Excel. Berkeley Geochronology Center Special Publication, *4*, 71.

McDougall, I., MacDougall, I., & Harrison, T. M. (1999). *Geochronology and Thermochronology by the ^{40}Ar/^{39}Ar method*. New York, NY: Oxford University Press.

Min, K., Mundil, R., Renne, P. R., & Ludwig, K. R. (2000). A test for systematic errors in ^{40}Ar/^{39}Ar geochronology through comparison with U/Pb analysis of a 1.1-Ga rhyolite. *Geochimica et Cosmochimica Acta*, *64*(1), 73–98. https://doi.org/10.1016/S0016-7037(99)00204-5

Renne, P. R., Deino, A. L., Hilgen, F. J., Kuiper, K. F., Mark, D. F., Mitchell, W. S., et al. (2013). Time scales of critical events around the Cretaceous-Paleogene boundary. *Science*, *339*(6120), 684–687. https://doi.org/10.1126/science.1230492

Renne, P. R., Swisher, C. C., Deino, A. L., Karner, D. B., Owens, T. L., & DePaolo, D. J. (1998). Intercalibration of standards, absolute ages and uncertainties in ^{40}Ar/^{39}Ar dating. *Chemical Geology*, *145*(1-2), 117–152. https://doi.org/10.1016/S0009-2541(97)00159-9

Steiger, R., & Jäger, E. (1977). Subcommission on geochronology: Convention on the use of decay constants in geo- and cosmochronology. *Earth and Planetary Science Letters*, *36*(3), 359–362. https://doi.org/10.1016/0012-821X(77)90060-7